

Material Matters™

VOLUME 16 • NUMBER 3

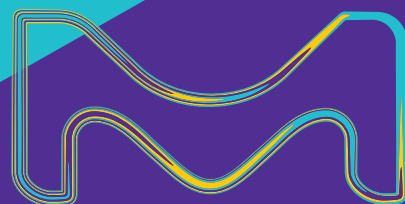
Smart Electronics

Recent Trends in Self-healing Soft
Electronic Materials and Devices

Stretchable Electroluminescent Devices

Van der Waals Heterostructures Down to
One Dimensional Level: Synthesis,
Characterization, and Applications

High Crystalline, Solution Processable
Organic Field Effect Transistors



Introduction



Monica Jung de Andrade, Ph.D.
Global Product Manager
– Electronic Materials
Materials Science

Welcome to issue 16.3 of *Material Matters*™, Smart Electronics. Materials in this exciting family of materials that can sense, adapt, actuate, or enable active control, allowing applications like stretchable and miniaturized devices and autonomous biosensing systems. This issue highlights recent trends associated with new material discoveries related to self-healing polymers, stretchable electroluminescent materials, one-dimensional van der Waals heterostructures, and organic field-effect transistors.

In our first article, **Professors Yu Jun Tan and Benjamin C.K. Tee** (National University of Singapore) review recent advances in self-healing polymers (SHP) for soft electronic materials and devices. They outline SHP classifications and applications, focusing on the vast applications within unpredictable working environments, cost reduction, and electronic waste mitigation.

In our second article, **Professor Qibing Pei** and colleagues (University of California - Los Angeles) examine advances in the transparent electrodes, electroluminescent (EL) materials, and device structures used in stretchable EL devices. While advances have been made in intrinsically stretchable materials for EL devices, the performance of these devices is still inferior to that of rigid EL devices in terms of turn-on voltage, efficiency, and lifetime. Thus, they emphasize the importance of parallel efforts on structure enabled focused, such as innovative designs that enable significant strain while keeping the non-emissive area small.

Professor Shigeo Maruyama (The University of Tokyo) and team describe how one-dimensional (1D) van der Waals heterostructures (vdWHs) are transforming the next generation of optoelectronics, in our third article. Here, Maruyama et al. describe how integration at the atomic scale combines with strong localized states at the submicron scale and provide an in-depth look at the existing 1D vdWHs while describing the technical and theoretical areas that need further development.

In our final article, **Professor Paddy Kwok Leung Chan** and colleagues (The University of Hong Kong) describe the latest advances in solution shearing organic field-effect transistor (OFET) devices. They highlight how the self-assembly of small molecule solutions may enable the next generation of biosensor devices, such as biocompatible and advanced miniaturized OFETs.

Each article in this publication concludes with a list of relevant Sigma-Aldrich® materials available from MilliporeSigma. For additional product information, please visit us at SigmaAldrich.com/matsci. We welcome novel product ideas! If you have any new product suggestions, questions or comments, or new ideas for future *Material Matters*™ issues, please contact us at SigmaAldrich.com/technicalservice.

About the Cover

This cover art depicts the best-known example from the animal kingdom of glowing and self-healing. Nature has inspired interdisciplinary development in smart electronics that encompass self-assembling small organic molecules, 1D nanomaterials enabling atomic integration, and self-healable, soft, and stretchable polymers. SigmaAldrich® Materials Science is dedicated to advancing the knowledge of nanomaterial technologies with a comprehensive portfolio of innovative materials to empower breakthroughs.



Merck KGaA, Darmstadt, Germany
Frankfurter Strasse 250
64293 Darmstadt, Germany
Phone +49 6151 72 0

To Place Orders / Customer Service

Contact your local office or visit
SigmaAldrich.com/order

Technical Service

Contact your local office or visit
SigmaAldrich.com/techinfo

General Correspondence

Contact your local office or visit
SigmaAldrich.com/techinfo

Subscriptions

Request your FREE subscription to *Material Matters*™ at SigmaAldrich.com/mm

The entire *Material Matters*™ archive is available at SigmaAldrich.com/mm

Material Matters™ (ISSN 1933-9631) is a publication of Merck KGaA, Darmstadt, Germany

Copyright © 2021 Merck KGaA, Darmstadt, Germany and/or its affiliates. All rights reserved. MilliporeSigma, the vibrant M, Sigma-Aldrich and Material Matters are trademarks of Merck KGaA, Darmstadt, Germany or its affiliates. All other trademarks are the property of their respective owners. Detailed information on trademarks is available via publicly accessible resources. More information on our branded products and services on MilliporeSigma.com

Table of Contents

Articles

Recent trends in Self-healing Soft Electronic Materials and Devices	3
Stretchable Electroluminescent Devices	9
Van der Waals Heterostructures down to One Dimensional Level: Synthesis, Characterization and Applications	18
High crystalline, solution processable organic field effect transistors	24

Featured Products

Autonomic Healing Systems A selection of materials for autonomic healing	7
Nonautonomic Healing Systems A selection of materials for nonautonomic healing	8
Electroluminescent Layer Products A selection of electroluminescent layer materials	14
Carbon Nanomaterials A selection of carbon nanomaterials for electroluminescent devices	15
PEDOT:PSS Materials A list of PEDOT:PSS materials for electroluminescent devices	15
Polyaniline Materials A list of polyaniline materials for electroluminescent devices	16
Polypyrrole Material A list of polypyrrole materials for electroluminescent devices	16
Fullerene A list of fullerenes for 1D vdWHs	22
Single Walled Carbon Nanotubes A selection of CNTs for 1D vdWHs	22
Monolayer Graphene A selection of graphene materials for 1D vdWHs	22
MAX phases A list of MAX phase materials for 1D vdWHs	23
Hexagonal Boron Nitride A list of hBN dispersions for 1D vdWHs	23
Printable Electrode Materials A selection of electrode materials for OFET	28
Organic Semiconducting Materials (Channel) A selection of channel materials for OFET	28

Your Material Matters

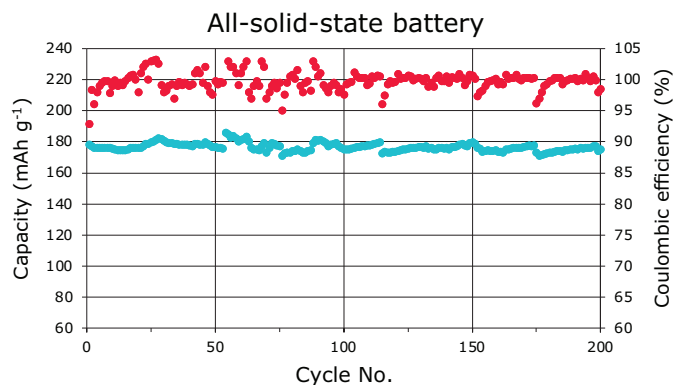


Bryce P. Nelson

Bryce P. Nelson, Ph.D.
Materials Science Initiative Lead

The development of organic-based electrodes for batteries has been an area of great interest due to their applications in flexible electronics. Polymer electrode materials demonstrate distinct advantages in material abundance, environmental friendliness, and structural diversity. However, the insulating nature of organic materials often results in sluggish electrochemical kinetics, thereby limiting their practical applications during high-power operation.

In collaboration with **Professor Deyang Qu** (University of Wisconsin - Milwaukee), our R&D team recently developed graphene polymeric nanocomposites for battery electrodes. By incorporating graphene sheets to form a nanocomposite, the achieved nanocomposites show greatly enhanced electronic conductivity. Under 10C, the cathode can still access 60% of its capacity at 0.1C. The feasibility of polymer/graphene nanocomposites (**921351**, **921386**, **921378**) has been validated in conventional batteries with liquid electrolytes and in the emerging all-solid-state batteries.



References

- (1) Song, Z.; Xu, T.; Gordin, M. L.; Jiang, Y.-B.; Bae, I.-T.; Xiao, Q.; Zhan, H.; Liu, J.; Wang, D. *Nano Lett.* **2012**, *12*, 2205. DOI: 10.1021/nl2039666
- (2) Song, Z.; Zhan, H.; Zhou, Y. *Angew. Chem. Int. Ed.* **2010**, *49*, 8444. DOI: 10.1002/anie.201002439
- (3) Muench, S.; Wild, A.; Friebe, C.; Häupler, B.; Janoschka, T.; Schubert, U. S. *Chem. Rev.* **2016**, *116*, 9438. DOI: 10.1021/acs.chemrev.6b00070

Name	Cat. No.
Reduced graphene oxide enhanced PAQS composite for battery	921351-1G
Reduced graphene oxide enhanced NTCDA composite for battery	921386-1G
Reduced graphene oxide enhanced PMDA composite for battery	921378-1G

From MAX Phase to MXene

MXene is a promising new family of 2D nanomaterials, consisting of conductive 2D carbides, nitrides, and carbonitrides.

First described by Professor Yury Gogotsi from Drexel University in 2011, MXenes combine both metallic conductivity and hydrophilic nature, due to their hydroxyl or oxygen terminated surfaces functional groups. They typically can be synthesized via top-down selective etching of their layered precursor materials, MAX phases.

MXene offers:

- High solution processability
- High conductivity
- High surface area
- High electrochemical activity

MXene are widely reported in applications such as:

- Conductive electronic devices
- Energy storage devices
- Sensors and biosensors
- Multifunctional composites
- Water purification
- Catalyst

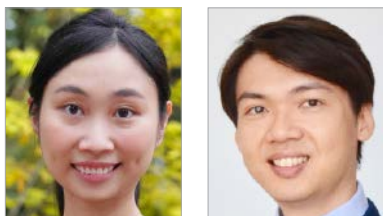
[SigmaAldrich.com/mxene](https://www.sigmaaldrich.com/mxene)



MilliporeSigma is
the U.S. and Canada
Life Science business
of Merck KGaA,
Darmstadt, Germany.

Sigma-Aldrich®
Lab & Production Materials

Recent trends in Self-healing Soft Electronic Materials and Devices



Yu Jun TAN,¹ Benjamin C.K. Tee²

¹ Mechanical Engineering, National University of Singapore

² Materials Science and Engineering, National University of Singapore

* Email: yujun.tan@nus.edu.sg, Benjamin.tee@nus.edu.sg

Introduction

Self-healing materials, inspired by biological systems, are capable of restoring some or most of their original properties when damaged without increasing their original mass.^{1,2} These state-of-the-art synthetic materials can be designed to self-recover from damages such as cuts, cracks, punctures, and impacts, either physically or chemically. Research shows these robust materials have the potential to extend the functional lifetime of materials and better ensure safety in the autonomous operations of electronics and machines.³

The healing efficiency, η , of the property of interest (P) of a self-healing material is quantifiable by:

$$\eta = \frac{P_{\text{healed}} - P_{\text{damaged}}}{P_{\text{pristine}} - P_{\text{damaged}}}$$

Where P can be mechanical, electrical, optical, or other properties.⁴ Compared to other self-healing materials, like metals and ceramics, the healing efficiency of self-healing polymers (SHPs) is superior, due to the high mobility of their polymeric chains. SHPs can be grouped according to three broad categories (**Figure 1**): inclusion of external healing agents, independence in self-healing activities, and class of polymers.

While autonomic SHPs restore their properties without external intervention in a self-contained manner, non-autonomic SHPs heal upon activation by specific external triggers such as thermal or chemical stimuli. The healing system in biomimetic autonomic SHPs is self-triggered once damage occurs, removing the need for exposure to external triggers. Some materials require gentle pressure to close up a wound for their autonomic self-healing and are considered in-between autonomic and non-autonomic self-healing.

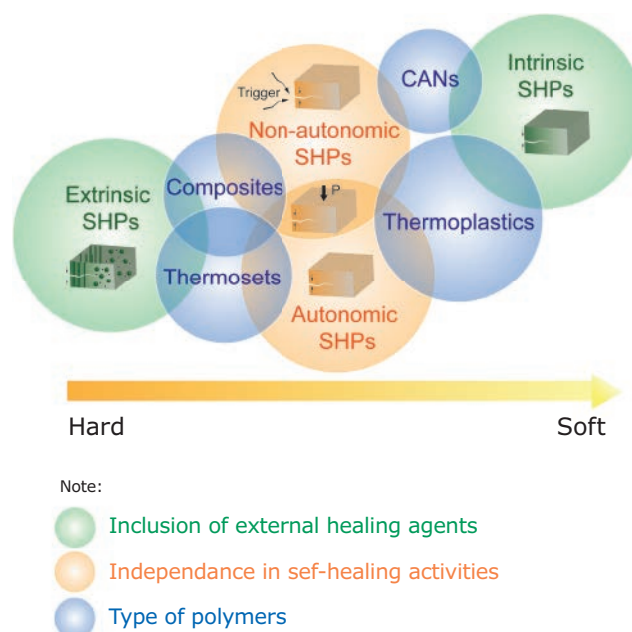


Figure 1. SHPs can be grouped according to three categories: inclusion of external healing agents: Intrinsic versus extrinsic SHPs; independence in self-healing activities: autonomic versus non-autonomic SHPs; type of polymers: thermosets, composites, covalent adaptable networks (CANs), or thermoplastics. The intrinsic SHPs are soft polymers, while the extrinsic SHPs are hard and strong polymers.

SHPs can heal either extrinsically or intrinsically. Extrinsic SHPs contain and utilize external healing agents, which can make integration of the healing agents complex. On the other hand, intrinsic SHPs initiate repair without relying on external healing materials and systems. Self-repair is achievable via the strong reversibility of molecular interactions within the intrinsic SHPs.

There are four classes of SHPs based upon polymer type.¹ Thermosets are insoluble and highly thermal stable, and usually require external healing agents to self-heal. For example, healing agents encapsulated in microcapsules or vascular systems rupture upon damage to release their payload. Polymers with covalent adaptable networks (CANs) or dynamic covalent bonds are thermosets with dynamic properties when triggered. CANs typically self-heal intrinsically but require external triggers.⁵ Non-covalent thermoplastics gain their strength from polymer chain entanglement and physical cross-linking. The self-healing mechanisms for thermoplastics can be intermolecular diffusion and intermolecular forces such as H-bond, dipole-dipole,⁶ van der Waals,⁷ ionic interactions,⁹ and coordination bonds,⁸ with or without external stimuli. Meanwhile, composite SHPs can be a physical blend of thermosets and thermoplastics or utilize shape memory materials and nanomaterials in the polymer matrix for self-healing. This group of materials is an example of extrinsic SHPs that can self-heal autonomously or non-autonomously.

In the last decade, elastomeric SHPs (Figure 2) have been used to enhance the durability of organic electronic devices (Figure 3) such as touch and pressure sensors,^{24–26} light-emitting devices,⁶ nanogenerators,²⁷ and energy storage devices.²⁸ Inspiration for the design of these self-healing technologies comes from the remarkable healing ability of human skin,²⁹ where catastrophic failure or fatigue in the synthetic materials can be self-repaired. Smart functional materials are a critical component of self-healing electronics.

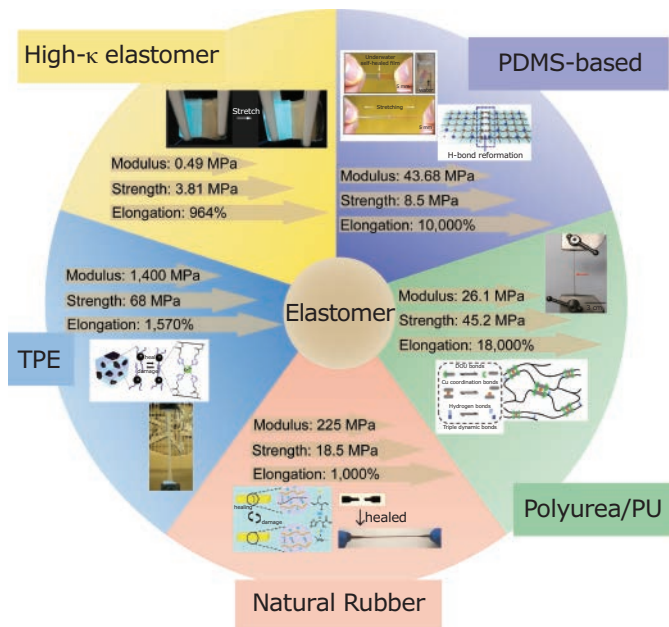


Figure 2. Examples of elastomeric SHPs. PDMS-based elastomer, polyurea/PU-based elastomer, natural rubber, thermoplastic elastomer (TPE), and high- κ elastomer. Values are extracted from references 9–18. Adapted with permission from reference 1, copyright 2020 Wiley-VCH; reference 19, copyright 2018 Wiley-VCH; reference 20, copyright 2019 Wiley-VCH; reference 21, copyright 2020 Elsevier; reference 22, copyright 2014 American Chemical Society; reference 23, copyright 2012 Springer Nature; and reference 6, copyright 2020 Springer Nature.

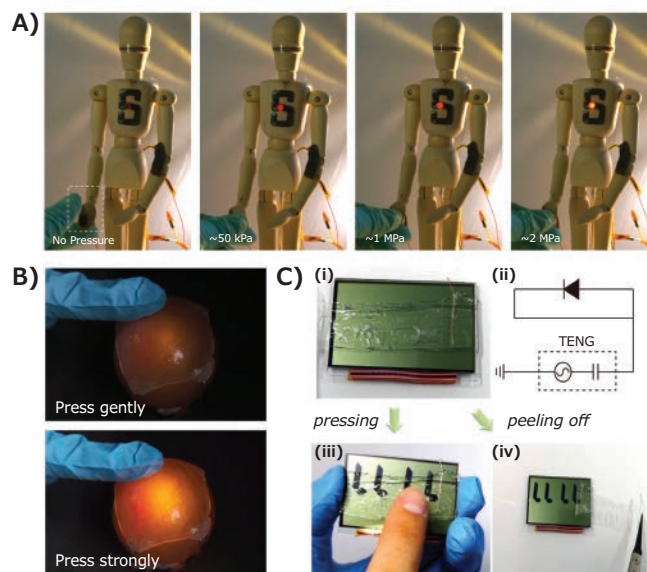


Figure 3. A–B) Photographs of self-healing pressure sensors. C), Images of a self-healing triboelectric nanogenerator. Adapted with permission from reference 24, copyright 2012 Springer Nature; reference 25 copyright 2019 Springer Nature; and reference 27, copyright 2020 American Chemical Society.

PVDF-based Self-healing Polymers and Their Applications

Self-Healing Dielectric Materials

A transparent, self-healing, stretchable PVDF-HFP-based dielectric with high permittivity (high- κ) was developed with permittivity values of 10 to 27, varying with frequency up to 10^5 Hz (Figure 4A).⁶ The amorphous PVDF-HFP-based self-healing dielectric material has a low glass transition temperature of -25°C affording high mobility to the polymer chains at room temperature. The strong yet reversible physical interactions within the SHP are due to hydrogen-fluorine intermolecular bond pairing, such as the strong dipole-dipole and van der Waals interactions, allowing the SHP to repeatedly self-heal.

The SHP is not sticky on its surface but is an intrinsic, autonomous self-healing thermoplastic with rapid self-healing. The healing efficiency, η , was 91% after 5 minutes of healing at room temperature, with near-complete healing in 24h when mildly heated to 50°C . The material can also self-heal at temperatures as low as -20°C due to the low glass transition temperature (Figure 4B).

This supramolecular dielectric polymer can be stretched elastically up to 20% and deformed plastically to $\sim 900\%$. With an ultimate tensile strength of 1.03 ± 0.02 MPa. Further enhancement of the elasticity of the polymer occurs via chemical cross-linking.^{6,32} Underwater self-healing can also occur by selecting polar hydrophobic small molecules that are miscible with the PVDF-HFP-based polymers.³³

Self-Healing Ionic Conductors

Transparent, ionically conductive PVDF-HFP-based polymers that can autonomously self-heal underwater can also be designed (Figure 4C,D).^{25,34} Self-healing happens via the highly reversible ion-dipole interaction between the ions and the polar fluorine molecules in the PVDF-HFP.

Unlike conventional electronic conduction, mobile ions drift from one end to another in ionic conduction systems while generating electrical conductivity. The ionic conductivity in this material system is tunable. Conductive atomic force microscopy (AFM) showed the change from discrete conductive droplets to a fully percolating phase in the ionic conductor when the concentration of the ions increased in the polymer matrix (Figure 4E).

It is crucial to develop self-healing conductors that quickly and effectively restore conductivity after damage and healing events. The ionic conductive PVDF-HFP-based polymer self-heals

electrically when two halves of damaged interfaces are placed back together upon slight contact.⁹ After 10 times cutting and healing, the polymer's healing efficiency in terms of conductivity was 90.7%. The mechanical self-healing efficiency in toughness was ~44% and ~99% after 1 day of healing under room temperature conditions and 50 °C.

When carefully paired between the ions and the base polymer, the self-healing ionic conductor has high transparency due to its strong intermolecular bonding.^{25,35,36} Moreover, submerging the hydrophobic ionic conductors in water does not change the appearance and electromechanical properties. The material self-heals when submerged in water, seawater, and acidic or basic solutions. The selected ions have high hydrophobicity that synergistically shielded themselves against the water molecules. As a result, these SHPs have comprehensive properties: high transparency, stability, stretchability, conductivity, hydrophobicity, and self-healing.

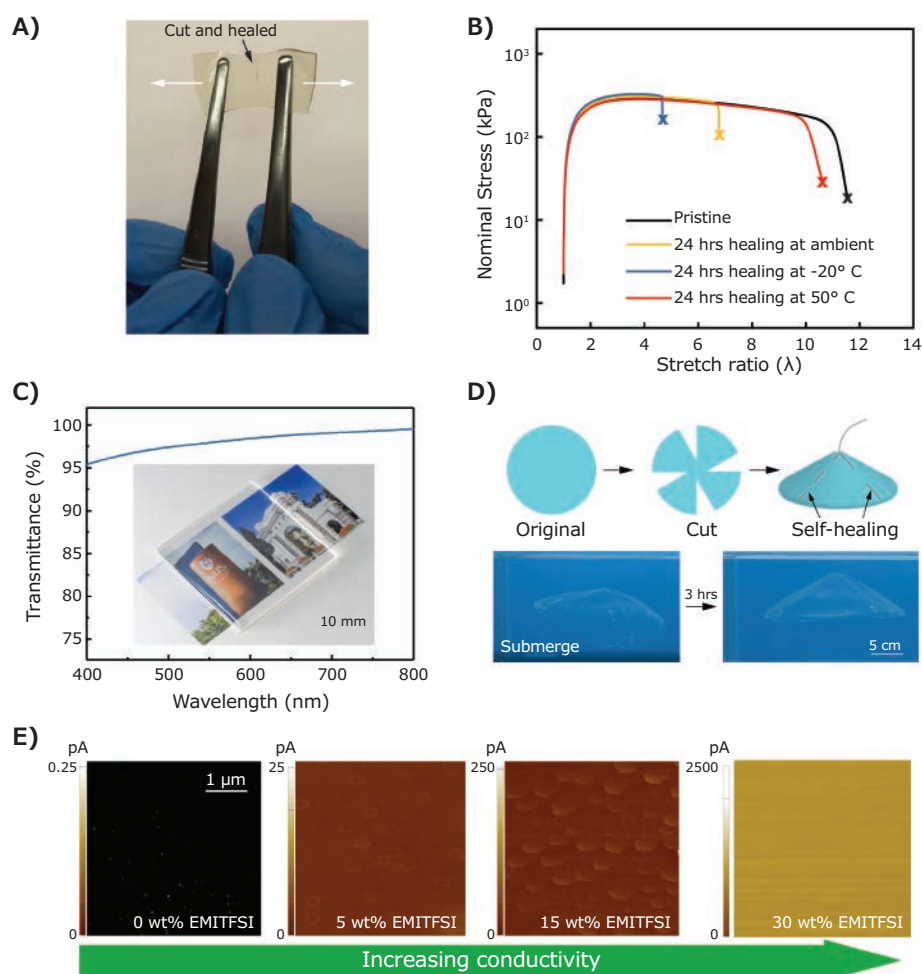


Figure 4. A) Photograph of a self-healing high- κ dielectric material. B) Graph showing self-healing in mechanical properties of the high- κ dielectric material at -20°C , room temperature and 50°C . C) Transmittance spectrum of a self-healing ionic conductor over the visible wavelengths of 400–800nm. Inset: photograph of the polymer film on a glass slide. D) Photographs show self-healed ionic conductors after submerging in water for 3 hours. The material retained its shape, self-healing capability, and transparency. E) Conductive AFM results show the transition from insulating to a percolating phase of ions in the PVDF-HFP-based polymer network. Adapted with permission from reference 6, copyright 2020 Springer Nature and reference 25, copyright 2019 Springer Nature.

Self-healing Devices Based on Transparent SHPs

SHPs with high healing efficiencies have numerous applications in soft electronics. Crucially, polymers that are highly stable, like the previously mentioned dielectric⁶ and ionic conductive²⁵ materials, are attractive for use in high-tech applications instead of self-healing polymers that can change their forms and properties over time.

Transparent SHPs have found application in various electronics and machines, especially in stretchable and self-healing touch screens and display screens. A highly transparent and stretchable capacitive touch screen that can self-heal autonomously was produced using ionically conductive materials;²⁵ the touch screen can even function and heal in water. The high transparency of the device allows for visible

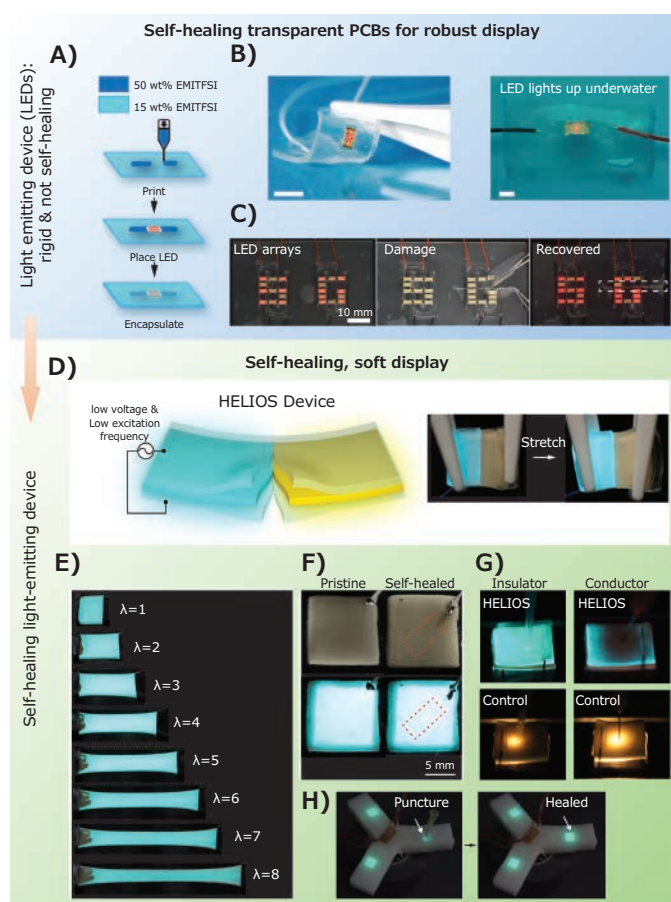


Figure 5. Photographs of self-healing displays. **A)** Schematic showing 3D printing of self-healing transparent PCBs with LEDs embedded. **B)** The conformable, soft, and transparent PCB can work underwater, and **C)** can recover from severe damages. **D)** HELIOS LEC device can be reconfigured by healing across blue and orange devices. **E)** HELIOS LEC can be stretched to 800% while illuminating. **F)** Photographs showing the HELIOS device can self-recover from severe cuts through all three layers of the LEC device. **G)** The HELIOS device could remain illuminated when puncturing with insulating or conducting sharp objects, while the control elastomeric LEC device sparked at the perforation point due to dielectric breakdown. **H)** Photograph showing HELIOS device embedded in a soft robot survived and healed from punctures. Adapted with permission from reference 1, copyright 2020 Wiley-VCH; reference 6, copyright 2020 Springer Nature; and reference 25, copyright 2019 Springer Nature.

and infrared light communication through the material. A transparent, soft, and self-healing printed circuit board (PCB) was 3D printed using the SHPs (Figure 5A–C).

Healable, low-field illuminating optoelectronic stretchable (HELIOS) light-emitting capacitors (LEC) have also been fabricated (Figure 5D,E).^{6,37} High transparency and high- κ dielectric material allows the HELIOS device to turn on at a much lower field and frequency. Most importantly, the capacitor is entirely self-healable from cuts and punctures (Figure 5F–H), and capable of restoring luminance within 5 min. The ability to self-heal from punctures during operation is in part due to its low operating fields and frequencies. In sharp contrast, a LEC made from a control elastomer requires operation at more typical higher field and frequency, and a prototype underwent dielectric breakdown when operated at these more typical operating conditions.

Summary

The emergence of smart, functional SHPs will be highly beneficial to the advancement of the next-generation self-healing soft electronic devices. Inspired by nature, SHPs demonstrate exciting opportunities for more reliable devices with utility in autonomous operations,^{38,39} especially in unpredictable working environments like the deep sea, internal body, or outer space. Autonomously self-healing devices could help to minimize the need for repair or replacement of electronics and machines, potentially reducing the cost of materials and reducing electronic waste. However, in the quest for bioinspired self-healing soft electronics and machines, smart, functional SHPs that are strong, compliant, stretchable, biocompatible, and self-healing at various length scales are still in high demand.

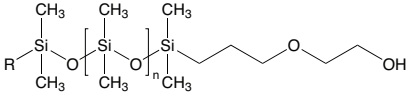
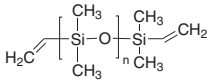
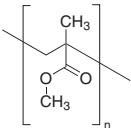
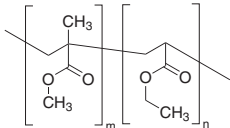
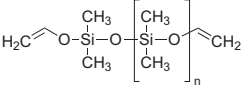
References

- (1) Tan, Y. J.; Susanto, G. J.; Anwar Ali, H. P.; Tee, B. C. K. *Adv. Mater.* **2020**, *33* (19), 2002800.
- (2) Kang, J.; Tok, J. B. H.; Bao, Z. *Nat. Electron.* **2019**, *2*, 144–150. <https://doi.org/10.1038/s41928-019-0235-0>.
- (3) Bartlett, M. D.; Dickey, M. D.; Majidi, C. *NPG Asia Mater.* **2019**, *11*, 1–4. <https://doi.org/10.1038/s41427-019-0122-1>.
- (4) Tan, Y. J.; Wu, J.; Li, H.; Tee, B. C. K. *ACS Appl. Mater. Interfaces* **2018**, *10* (18), 15331–15345. <https://doi.org/10.1021/acsami.7b19511>.
- (5) Wang, S.; Urban, M. W. *Nat. Rev. Mater.* **2020**, *5*, 562–583. <https://doi.org/10.1038/s41578-020-0202-4>.
- (6) Tan, Y. J.; Godaba, H.; Chen, G.; Tan, S. T. M.; Wan, G.; Li, G.; Lee, P. M.; Cai, Y.; Li, S.; Shepherd, R. F.; Ho, J. S.; Tee, B. C. K. *Nat. Mater.* **2020**, *19* (2), 182–188. <https://doi.org/10.1038/s41563-019-0548-4>.
- (7) Urban, M. W.; Davydovich, D.; Yang, Y.; Demir, T.; Zhang, Y.; Casabianca, L. *Science* **2018**, *362* (6411), 220–225. <https://doi.org/10.1126/science.aat2975>.
- (8) Li, C.; Zuo, J. *Adv. Mater.* **2019**, *32* (27), 1903762. <https://doi.org/10.1002/adma.201903762>.
- (9) Sattar, M. A.; Gangadharan, S.; Patnaik, A. *ACS Omega* **2019**, *4*, 10939–10949.
- (10) Rhaman, M. A.; Penco, M.; Spagnoli, G.; Grande, A. M.; Di Landro, L. *Macromol. Mater. Eng.* **2011**, *296*, 1119–1127.
- (11) Mugesana, C.; Grysan, P.; Dieden, R.; Ruch, D.; Bruns, N.; Dubois, P. *Macromol. Chem. Phys.* **2020**, *221*, 1–6. <https://doi.org/10.1002/macp.201900432>.
- (12) Zhang, Y. et al. *Adv. Mater.* **2016**, *28*, 7646–7651. <https://doi.org/10.1002/adma.201601242>.
- (13) Lai, J.-C.; Jia, X.-Y.; Wang, D.-P.; Deng, Y.-B.; Zheng, P.; Li, C.-H.; Zuo, J.-L.; Bao, Z. *Nat. Commun.* **2019**, *10*, 1–9. <https://doi.org/10.1038/s41467-019-09130-z>.
- (14) Madsen, F. B.; Yu, L.; Skov, A. L. *ACS Macro Lett.* **2016**, *5*, 1196–1200.
- (15) Xu, J. H.; Chen, W.; Wang, C.; Zheng, M.; Ding, C. D.; Jiang, W.; Tan, L. H.; Fu, J. J. *Chem. Mater.* **2018**, *30* (17), 6026–6039. <https://doi.org/10.1021/acs.chemmater.8b02320>.

- (16) Zhang, L.; Wang, D.; Xu, L.; Zhang, X.; Zhang, A., Xu, Y. *J. Mater. Chem. C* **2020**, *8*, 2043–2053.
- (17) Bao, Z. et al. *Nat. Chem.* **2016**, *8*, 618–624.
- (18) Yanagisawa, Y.; Nan, Y.; Okuro, K.; Aida, T. *Science* **2018**, *359*, 72–76.
- (19) Kang, J.; Bao, Z.; et al. *Adv. Mater.* **2018**, *30*, 1706846. <https://doi.org/10.1002/adma.201706846>
- (20) Zhang, L. et al. *Adv. Mater.* **2019**, *31*, 32–34. <https://doi.org/10.1002/adma.201901402>
- (21) Yang, X.; Liu, J.; Fan, D.; Cao, J.; Huang, X.; Zheng, Z.; Zhang, X. *Chem. Eng. J.* **2020**, *389*, 124448. <https://doi.org/10.1016/j.cej.2020.124448>
- (22) Mozhdzhi, D.; Ayala, S.; Cromwell, O. R.; Guan, Z. *J. Am. Chem. Soc.* **2014**, *136*, 16128–16131.
- (23) Chen, Y.; Kushner, A. M.; Williams, G. A.; Guan, Z. *Nat. Chem.* **2012**, *4*, 467–472.
- (24) Tee, B. C. K.; Wang, C.; Allen, R.; Bao, Z. *Nat. Nanotechnol.* **2012**, *7*, 825–832.
- (25) Cao, Y.; Tan, Y. J.; Li, S.; Lee, W. W.; Guo, H.; Cai, Y.; Wang, C.; Tee, B. C. K. *Nat. Electron.* **2019**, *2*, 75–82.
- (26) Khatib, M.; Zohar, O.; Haick, H. *Adv. Mater.* **2021**, *33* (11), 2004190. <https://doi.org/10.1002/adma.202004190>
- (27) Chen, H.; Koh, J. J.; Liu, M.; Li, P.; Fan, X.; Liu, S.; Yeo, J. C. C.; Tan, Y.; Tee, B. C. K.; He, C. *ACS Appl. Mater. Interfaces* **2020**, *12*, 31975–31983.
- (28) Mai, W., Yu, Q., Han, C., Kang, F. & Li, B. Self-Healing Materials for Energy-Storage Devices. *Adv. Funct. Mater.* *30*, 1909912 (2020).
- (29) Benight, S. J.; Wang, C.; Tok, J. B. H.; Bao, Z. *Prog. Poly. Sci.* **2013**, *38*, 1961–1977.
- (30) Ameduri, B. *Chem. Rev.* **2009**, *109*, 6632–6686.
- (31) Martins, P.; Lopes, A. C.; Lanceros-Mendez, S. *Prog. Poly. Sci.* **2014**, *39*, 683–706.
- (32) Guo, H.; Tan, Y. J.; Chen, G.; Wang, Z.; Susanto, G. J.; See, H. H.; Yang, Z.; Lim, Z. W.; Yang, L.; Tee, B. C. K. *Nat. Commun.* **2020**, *11*, 1–10.
- (33) Cao, Y. Wu, H.; Allec, S. I.; Wong, B. M.; Nguyen, D.-S.; Wang, C. *Adv. Mater.* **2018**, *30*, 1804602. <https://doi.org/10.1002/adma.201804602>
- (34) Majidi, C. *Nat. Electron.* **2019**, *2*, 58–59.
- (35) Cao, Y. Morrissey, T. G.; Acome, E.; Allec, S. I.; Wong, B. M.; Keplinger, C.; Wang, C. *Adv. Mater.* **2017**, *29*, 1605099. <https://doi.org/10.1002/adma.201605099>
- (36) Zhang, Y.; Li, M.; Qin, L.; Chen, L.; Liu, Y.; Zhang, X.; Wang, C.; *Chem. Mater.* **2020**, *32*, 6310–6317.
- (37) Rossiter, J. *Nat. Mater.* **2020**, *19*, 134–135.
- (38) Pena-Francesch, A.; Jung, H.; Demirel, M. C.; Sitti, M. *Nat. Mater.* **2020**, *19*, 1230–1235.
- (39) Khatib, M.; Zohar, O.; Saliba, W.; Haick, H. A. *Adv. Mater.* **2020**, *32*, 2000246.

Autonomic Healing Systems

Name	Structure	Purity, Molecular Weight	Cat. No.
5-Norbornene-2,2-dimethanol		98%	152188-1G
Octamethylcyclotetrasiloxane		98%	235695-25G 235695-100G
Poly(dimethylsiloxane)		-	469319-50ML
Poly(dimethylsiloxane), bis(3-aminopropyl) terminated		average $M_n \sim 2,500$	481688-10ML 481688-50ML
Poly(dimethylsiloxane), diglycidyl ether terminated		average $M_n \sim 800$	480282-50ML 480282-250ML
Poly(dimethylsiloxane-co-diphenylsiloxane), dihydroxy terminated		-	482153-25ML
Poly(dimethylsiloxane-co-diphenylsiloxane), divinyl terminated		average $M_n \sim 9,300$	482048-25ML
Poly(dimethylsiloxane), hydroxy terminated		average $M_n \sim 550$	481939-100ML 481939-500ML
		-	432989-100ML 432989-500ML
		-	432997-100ML 432997-500ML
		average $M_n \sim 110,000$	482005-100ML
Poly(dimethylsiloxane-co-methylhydrosiloxane), trimethylsilyl terminated		average $M_n \sim 950$	482196-50ML
		average $M_n \sim 13,000$	482374-25ML 482374-150ML

Name	Structure	Purity, Molecular Weight	Cat. No.
Poly(dimethylsiloxane), monohydroxy terminated	 <p>R=Alkyl(methyl or butyl)</p>	average $M_n \sim 4,670$	480355-50ML
Poly(dimethylsiloxane), vinyl terminated		average $M_w \sim 25,000$	433012-100ML 433012-500ML
Poly(methyl methacrylate)		average $M_w \sim 15,000$ by GPC average $M_w \sim 120,000$ by GPC average $M_w \sim 350,000$ by GPC	200336-50G 200336-100G 182230-25G 182230-500G 182230-1KG 445746-25G 445746-500G 445746-1KG
Poly(methyl methacrylate-co-ethyl acrylate)		average $M_n \sim 39,500$ by GPC average $M_w \sim 101,000$ by GPC	182249-25G 182249-1KG
SYLGARD® 184		-	761036-5EA
SYLGARD® 186		-	901142-5EA

Nonautonomic Healing Systems

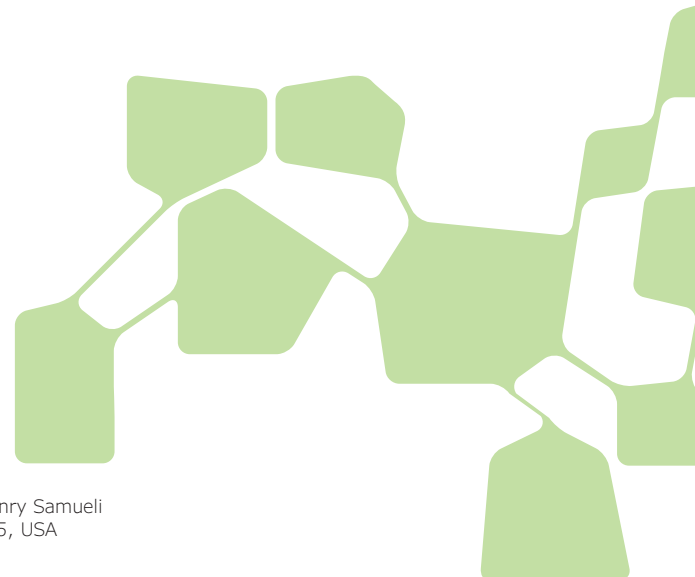
Name	Purity	Form,	Cat. No.
4-[(S,S)-2,3-Epoxyhexyloxy]phenyl 4-(decyloxy)benzoate	98%	liquid crystal	328537-100MG
4'-Heptyl-4-biphenylcarbonitrile	98%	liquid crystal	330817-1G
4'-(Hexyloxy)-4-biphenylcarbonitrile	96%	liquid crystal (nematic)	338656-1G
4'-Hydroxy-4-biphenylcarbonitrile	97%	liquid crystal	374784-1G 374784-5G
11-Maleimidoundecanoic acid	95%	powder	755850-25G
4-Octylbenzoic acid	99%	liquid crystal	374202-1G

Stretchable Electroluminescent Devices



Hexing Yin, Qibing Pei

Soft Materials Research Laboratory, Department of Materials Science and Engineering, Henry Samueli School of Engineering and Applied Science, University of California, Los Angeles, CA 90015, USA
* E-mail: qpei@seas.ucla.edu



Introduction

Electroluminescent (EL) devices date back more than a century ago, to when H. J. Round applied an electrical bias on a carborundum crystal and observed a yellowish glow. Since then, many materials have been investigated for use in fabricating EL devices. Today, displays based on organic light-emitting diodes (OLEDs) proliferate the consumer market, from watches to large-screen television sets. The latest OLED displays provide enhanced efficiency, color range, and lifetime. Besides these performance metrics, deformability has been gaining increasing attention for EL devices. Deformable displays are poised to create new opportunities in the automotive and mobile device industry. Conventional EL devices have limited deformability due to the rigidity of both the EL materials and electrodes. In 1992, the first flexible OLED was reported using conductive polyaniline (PANI, **Cat. No. 912891**) on polyethylene terephthalate (PET) substrate as the anode, poly[2-methoxy-5-(2-ethylhexyloxy)-1,4-phenylenevinylene] (MEH-PPV, **Cat. No. 541435**) as EL layer, and calcium as the cathode.¹ The multilayer thin film structure based primarily on polymers was the key to achieving its flexibility. Through tremendous efforts in the following 30 years, numerous companies have developed prototypes of flexible displays that can be bent, folded, or even rolled up. Samsung and Huawei have recently introduced smartphones with a foldable OLED display screen.

Researchers are now working to further stretch the deformability spectrum by developing EL devices that can be elongated. Unlike flexible devices, which only need to bear a few percent of bending strain, stretchable devices must undergo at least 10% strain and can thus be twisted, crumpled, and expanded to increase the display area. The high mechanical compliance may be uniquely suitable for conformably attaching electronic devices to dynamic and curvilinear surfaces.² For

example, while wearable devices like smartwatches today are still rigid and bulky, future smartwatches with stretchable displays may be worn as a wrist band and can deform along with skin to offer intimate human-machine communication. However, despite the high demand and enthusiasm, challenges remain to simultaneously achieve high stretchability and high device performance.

There are two general categories of stretchable EL devices to achieve stretchability. One is enabled through novel geometry and structure, which typically comprise discrete rigid EL elements and stretchable interconnects. The other type is an intrinsically stretchable EL device where all key materials in the devices are stretchable. Our group demonstrated an intrinsically stretchable polymer light-emitting electrochemical cell (PLEC) and a polymer OLED (PLED). Many other groups have also reported stretchable OLEDs and phosphor particle-elastomer-based EL devices. Performance of these devices still lags behind those rigid EL devices in terms of turn-on voltage, efficiency, and lifetime. Various new materials and architectures are under development. This review offers a concise survey of the representative stretchable EL devices focusing on the key elements: electrode, EL material, and device structure.

Electrode

A wide variety of conductive materials have been explored as candidates for the electrodes of stretchable EL devices. Traditional electrode materials like gold (Au), silver (Ag), and indium tin oxide (ITO, **Cat. No. 747939**) usually crack when stretched by 5% if no stretchable geometrical design is implemented.³ Thus, developing new electrodes of low sheet resistance ($< 100 \text{ Ohm sq}^{-1}$), high transparency ($> 80\%$), and high stretchability ($> 20\%$ strain) represents a significant effort

of the field. A general strategy to introduce stretchability is to construct percolation networks of nanometer-scale conductive materials in an elastomer matrix. Nanoparticles (0D), nanowires (1D), and nanoflakes/nanosheets (2D) have all been considered. Among these, nanowires usually exhibit the best performance in terms of conductivity, transmittance, and stretchability, owing to their high length-to-diameter aspect ratio, which allows the formation of numerous contact junctions on each nanowire. Thus, forming a percolation network at low filler loading. Such a percolation network has large openings to transmit light, leading to high optical transmittance. Silver nanowires (AgNW, **Cat. No. 778095**) and carbon nanotubes (CNT, **Cat. No. 791504**) are among the most widely used 1D conductive fillers. They may be dispersed in common solvents, like water and isopropanol and coated on desired substrates via vacuum filtration, screen printing, spraying, spin-coating, bar, and dip coating. There is a tradeoff between sheet resistance and optical transmittance, and this can be balanced depending on specific application requirements.

Uniformly blending the nanomaterials in an elastomer is one option for making stretchable interconnects.⁴ For transparent electrodes, attaching the nanomaterials to the surface or embedding in the surface layer of an elastomer is preferred. Such bilayer heterogeneous structures minimize the conductive materials required in the electrode to maintain optical transparency. This also allows the network to be patterned by dry etching, wet etching, or laser ablation. Embedding a conductive network in an elastomer surface layer reduces the surface roughness so that thin-film electronics can be fabricated on the electrode; this is significant for the fabrication of OLED devices where the emissive semiconductor layer is merely 100 nm thick. For example, Yu et al. fabricated the single-wall carbon nanotube-poly(tert-butyl acrylate) (SWCNT-PtBA) composite electrode and demonstrated the first intrinsically stretchable PLEC.⁵ In their experiment, SWCNTs were first bar-coated on glass and infiltrated by tert-butyl acrylate monomer,

followed by polymerization via ultraviolet (UV) light exposure. Then, the PtBA film was peeled off from the glass substrate, and the SWCNT network was buried in the polymer surface (**Figure 1A and 1B**). The figure of merit transmittance was 87% at 550 nm wavelength with 500 Ohm sq⁻¹ sheet resistance. The average surface roughness was less than 10 nm.

PtBA is a shape memory polymer that can stretch the composite electrode by 50% strain at an elevated temperature with little sheet resistance change. Liang et al. subsequently developed a AgNW-poly(urethane acrylate) (PUA) composite electrode via a similar transfer approach.⁶ Admixing PUA with an ethoxylated bisphenol A dimethacrylate monomer in the formulation obtained both high elongation (~150 %) and good bonding force with AgNWs (**Figure 1C and 1D**). Compared to the SWCNT-PtBA electrode, the AgNW-PUA electrode provided lower sheet resistance (15 Ohm sq⁻¹) at comparable transmittance (83% at 550 nm) and lower surface roughness (peak to valley value being 3.4 nm). The sheet resistance of the AgNW-PUA electrode increased by 23 times when the electrode was stretched to 100 % strain. In 1400 cycles of repeated stretching to 30 % strain, the electrode resistance increased from 15 Ohm sq⁻¹ to 65 Ohm sq⁻¹, but it recovered to 45 Ohm sq⁻¹ after 30 min of idle time at the relaxed state.

Besides the nanomaterial/elastomer composites, doped conjugated polymers have also been modified for stretchable transparent electrodes. PANI, polypyrrole (PPy, **Cat. No. 577030**), and poly(3,4-ethylenedioxythiophene):poly styrene sulfonate (PEDOT:PSS, **Cat. No. 655201**) are good examples. High conductivity is usually derived from dense and ordered packing of the conjugated polymer chains for such conductive polymers, and such microstructures diminish deformability. PEDOT:PSS, for instance, cannot survive more than 5% strain itself.⁷ An effective strategy is to mix the conductive polymers with a small molecule or polymer of high stretchability. Bade et al. mixed PEDOT:PSS with polyethylene oxide (PEO) to form a homogeneous solution, then spin-coated on a polydimethylsiloxane (PDMS) substrate.⁸ Interestingly, adding a small amount of PEO raised the conductivity of PEDOT:PSS. It is suggested that PEO might screen the Coulombic interaction between PEDOT and PSS. Phase segregation occurs where PEDOT chains change from coil to extended coil or linear.⁹ At 33 wt% loading of PEO, the PEDOT:PSS-PEO blend electrode showed 82% transmittance at 550 nm and 140 Ohm sq⁻¹ (**Figure 2A and 2B**). The electrode could be stretched up to 40% strain with a 12% increase in resistance. Wang et al. formulated a highly stretchable and conductive PEDOT:PSS composite by incorporating ionic additives with sulfonate or sulfonamide anions (**Figure 2C**).⁴ These additives enhanced the stretchability and electric conductivity by weakening the interaction between PEDOT and PSS. PEDOT domains aggregated to form conductive pathways within the softened PSS matrix. Transmittance of 96% at 550 nm was obtained with 59 Ohm sq⁻¹ (**Figure 2D**), achieving a conductivity of 4100 S cm⁻¹ at 100% strain.

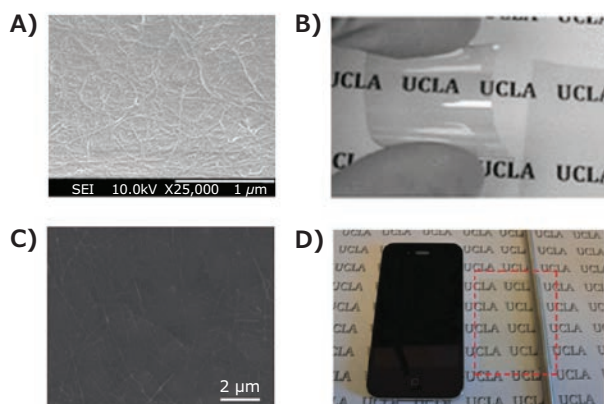


Figure 1. A) SEM image of conductive surface of the SWCNT-PtBA electrode, B) photograph of 500 Ohm sq⁻¹ SWCNT-PtBA electrode, C) SEM image of conductive surface of the AgNW-PUA electrode, D) photograph of 15 Ohm sq⁻¹ AgNW-PUA electrode

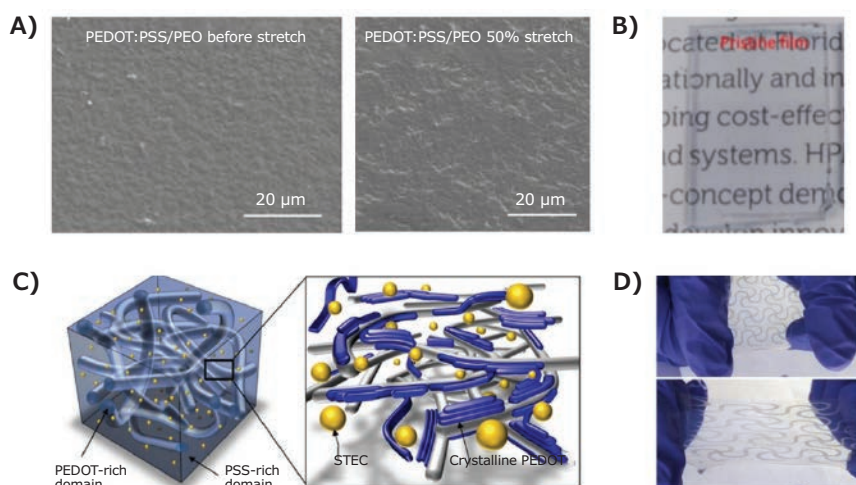


Figure 2. A) SEM images and B) Photographs of conductive surfaces of the PEDOT:PSS-PEO electrode. C) Schematic diagram representing the morphology of a stretchable PEDOT film with STEC enhancers. D) Patterned PEDOT/STEC film on SEBS (top) and stretching the film (bottom).

Ionic hydrogel can be used as the electrode in stretchable alternating current electroluminescence (ACEL) devices. Unlike PLED or PLEC, where electrons and holes are injected and recombine radiatively in the EL layer, ACEL devices generate light by a different mechanism: charge carriers are injected and accelerated in the EL layer at a high electric field, which then impacts and excites the luminescent center, where light is generated after radiative relaxation. This mechanism allows the use of low conductive electrodes in the ACEL devices. Ionic hydrogel has high transparency (~100% in the visible spectrum), low modulus, large stretchability (> 600% strain), and a small resistance increase during stretching. However, solvent or liquid in hydrogel evaporates rapidly, causing packaging and durability concerns. Larson et al. employed lithium chloride (LiCl) dissolved in a polyacrylamide (PAM) hydrogel on Ecoflex as the electrode to fabricate a hyperelastic light-emitting capacitor.¹⁰ They chose LiCl because of its moderate conductivity (~10 S m⁻¹), ionic strength, and hygroscopic nature (helps retain water). PAM was used as a matrix due to its high toughness and high transparency. The resulting electrode had a maximum strain of 500%. The resistance increased over 400% strain was just 2.5 times that of the original value.

EL material

Emissive materials in stretchable EL devices vary along with the device category. Intrinsically stretchable light-emitting polymers (LEPs) are desired for stretchable PLED devices. Ideally, such polymers should have ambipolar charge carrier mobility, high electroluminescence quantum yield, narrow emission peak in the visible spectrum, and high stretchability. Nevertheless, semiconducting polymers with extended p-electron conjugation usually exhibit semi-crystallinity due to strong π - π stacking between neighboring chains and poor stretchability.¹¹ Liang et al. demonstrated an intrinsically stretchable PLED with a blend of 1,3-bis[(4-tert-butylphenyl)-1,3,4-oxadiazolyl]phenylene (OXD-7)

and a white LEP provided by Cambridge Display Technology, Ltd. The resulting device was soft, looked like a piece of rubber sheet, was turned on at 7 V. A high brightness of 1100 cd m⁻² was obtained at 21 V, with a reported maximum current efficiency of 4.0 cd A⁻¹.¹²

Another approach is blending EL polymers with additives like a small molecule, elastomer, and ionic liquid. A good example is the EL layers in the PLEC, comprising a conjugated polymer, salt, and ionic conductor. Liang et al. blended a phenyl substituted poly(1,4-phenylenevinylene) (Super yellow light-emitting PPV copolymer, **Cat. No. 900438**), ethoxylated trimethylolpropane-tri acrylate (ETPTA, **Cat. No. 412198**), PEO, and lithium trifluoromethane sulphonate (LiTF) for the stretchable PLEC emissive layer.⁶ While SuperYellow is stiff, the ionic conductive medium is soft and forms a dispersed phase in the SuperYellow matrix. The blend as a whole could be stretched like a sponge.¹³

Perovskite nanocrystal-polymer composites may also be made stretchable, as shown by Bade et al., who mixed methylammonium lead tribromide (MAPbBr₃) crystals with PEO as the emissive layer (**Figure 3A**).⁸ The perovskite crystals were found densely distributed in the PEO matrix (**Figure 3B**). This homogeneous, pin-hole-free composite film can be stretched to 50% strain.

Doped with metals like copper or manganese, ZnS phosphor powders blended with an elastomer are frequently used as EL materials in stretchable ACEL devices. To accommodate the large size of phosphor powder (diameter ~ 20 μ m) and to avoid device breakdown under significant bias, the ACEL devices usually use a thick emissive layer (> 50 μ m, sometimes even a few mm). The emission color can be easily tuned via dopants in ZnS. Silicone such as PDMS (**Cat. No. 761036**) and Ecoflex are favorable elastomer matrices used in ACEL devices due to their excellent stretchability and easy-handing. For example, Larson

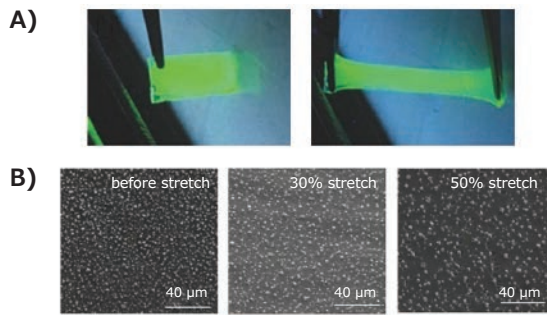


Figure 3. A) Photos of the MAPbBr₃/PEO composite film under 365 nm UV irradiation before and after stretching to ~100% strain. B) SEM images of the MAPbBr₃/PEO composite thin film stretched to 0, 30%, and 50% strain.

et al. employed a 1 mm thick film of a homogenous dispersion of 25 μm diameter ZnS powders in Ecoflex 00-30.¹⁰ The resulting hyperelastic light-emitting capacitor had a maximum stretchability of 487% strain. Red, green, and blue pixels were all demonstrated.

Structure-Enabled Stretchable EL Devices

Two categories of structure-enabled stretchable EL devices have been studied. One is the island-bridge structure. As the name suggested, patterned serpentine or “wavy” structures are introduced as bridges to connect rigid LED islands on an elastomer substrate. The serpentine structures deform geometrically within or out of the elastomer surface during stretching, while the rigid LEDs experience minor strain and maintain high diode performance (Figure 4A).¹⁴ One advantage of the island-bridge approach is that the conventional fabrication process fabricates the rigid EL components. A drawback of this approach is the sophisticated geometry designs of the interconnects, which incur complex fabrication routes. The dot pitch cannot be shrunk to display high-resolution images, as the rigid LEDs do not deform. The elastic spacing between them needs to be significant to obtain a sizeable overall deformation.¹⁵ Managing the strain distribution at the serpentine/island interface is also challenging.

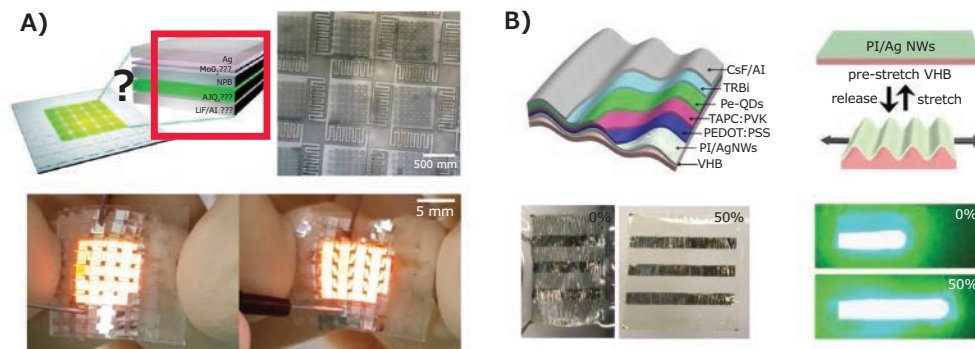


Figure 4. A) Typical geometric design and device performance under stretching of the island-bridge structure. B) Device structure and performance under stretching of the buckled MAPbBr₃ QLED.

The other type of structure-enabled stretchability can be realized by attaching a pre-fabricated ultrathin flexible EL device onto a pre-stretched elastomer substrate. After releasing the strain, the flexible EL device buckles out of plane to form a periodical wrinkle structure. Large-strain deformation is accommodated by un-wrinkling or bending deformation of the EL layer. Repeated stretching can be tolerated as the ultrathin EL device bends and flattens on the elastomer substrate. Li et al. demonstrated a stretchable perovskite QLED via this wrinkle structure method (Figure 4B).¹⁶ In this work, an ultrathin (~2 μm) QLED was first built on glass and then attached to a pre-stretched VHB elastomer, using MAPbBr₃ QDs as the emissive layer. The device had a low turn-on voltage of 3.2 V, maximum current efficiency of 9.2 cd A⁻¹, peak brightness of 3187 cd m⁻² at 9 V, and maximum linear strain of 50%. After 1000 cycles of repeated stretch to 20% strain, the device showed minimal performance fluctuation. A critical aspect of this approach is to obtain buckles of the appropriate wavelength. Macroscopic wrinkles with wavelengths of hundreds of microns are relatively easy to obtain but are visible to the naked human eye. Buckles of small wavelength, on the other hand, have a small bending radius and can cause significant strain in the rigid emissive layers.

Intrinsically Stretchable EL Devices

Intrinsically stretchable EL devices reported so far include PLEDs, PLECs, perovskite-polymer LEDs, and ACEL devices. These devices overcome the disadvantages of low effective area and complex fabrication found with the structure-enabled stretchable EL devices. Stretchable PLED demonstrated by Liang et al. shared similar multi-stack thin-film architectures as conventional OLEDs (Figure 5A).¹² In this work, PEDOT:PSS was spin-coated on AgNW-PUA anode as the hole injection layer (HIL). It also shielded solvent attack in the subsequent spin coating of the white LEP blended with OXD-7. Polyethylenimine (PEI, Cat. No. 408719) was spin-coated on another AgNW-PUA electrode to boost electron injection (EIL). The two AgNW-PUA films with respective polymer coatings were laminated together to complete the device fabrication. The device could be stretched by as much as 130% strain, which was irreversible. It could be stretched repeatedly at 40% strain for 100 cycles.

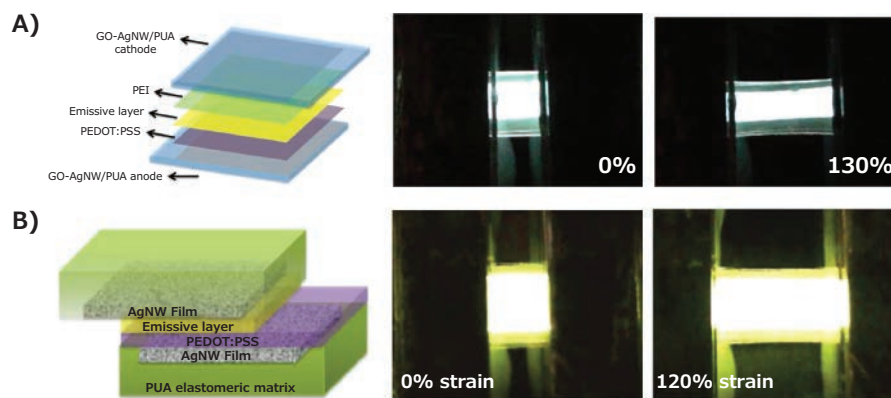


Figure 5. Structures and performances of the intrinsically stretchable A) PLED and B) PLEC.

HIL and EIL layers in the PLED are required to overcome hole and electron and injection barriers at the anode and cathode interfaces, respectively. These layers, as well as the EL layer, must be ultrathin to keep driving voltage low. The lamination may cause pinholes and other defects in the layers. These issues are relieved in PLECs, where forming a p-i-n junction in the emissive layer promotes charge injections without the HIL and EIL layers and allows a relatively thick EL layer.¹⁷ The stretchable PLEC demonstrated by Liang et al. was made by simply spin coating a homogenous solution of Super yellow light-emitting PPV copolymer, PEO, ETPTA, and LiTf on AgNW-PUA electrode and laminating this with another AgNW-PUA electrode (Figure 5B).⁶ The device showed a 6.8 V turn-on voltage, 2200 cd m⁻² maximum brightness at 21 V, 5.7 cd A⁻¹ maximum current efficiency, and stretchability up to 120% strain. It could be repeatedly stretched to 30% strain for 1000 cycles. Recently, Liu et al. demonstrated a fully stretchable active-matrix PLEC.¹⁸

The PLEC architecture does introduce new issues. One is finding a solvent that can dissolve the conjugated polymer, salt, and ionic conductor. Such solvent can typically cause swelling or cracking of the elastomeric polymer substrate. Re-transferring the PLEC layer formed on a release substrate onto the stretchable electrode creates new challenges. Stretchable ACEL devices of similar architecture, however, experience less solvent attacking issues. The EL layers of ACEL devices are tens or hundreds of microns thick, which simplifies the device fabrication. Free-standing films of the EL layer and electrodes may be produced separately and then laminated together. The large thickness does lead to high driving voltage (> 100 V) and high alternating frequency (> 1 kHz). Additionally, the brightness of the ACEL devices was low. Tan et al. mixed a fluoroelastomer, poly(vinylidene fluoride-co-hexafluoropropylene) (P(VDF-HFP)), with a small amount of FS-300 as the elastomer matrix with both high dielectric permittivity and stretchability to address these issues.¹⁹ The same fluoroelastomer with an ionic liquid, 1-ethyl-3-methylimidazolium bis(trifluoromethylsulfonyl) imide (EMITFSI, Cat. No. 11291), added was used as the electrodes. The resulting ACEL device was self-healing. The device showed a turn-on voltage of 23 V with an alternating frequency below

1 kHz, maximum brightness of 1460 cd m⁻² at 3750 V, and a giant stretchability of 800% strain, allowing for repeated stretching at 20% strain for 1000 cycles.

Conclusion

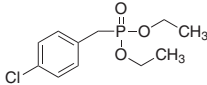
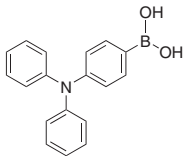
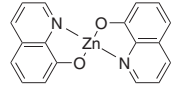
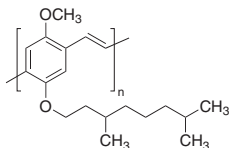
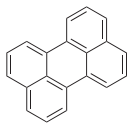
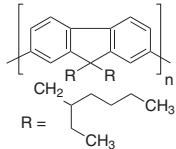
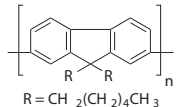
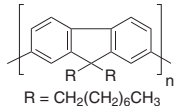
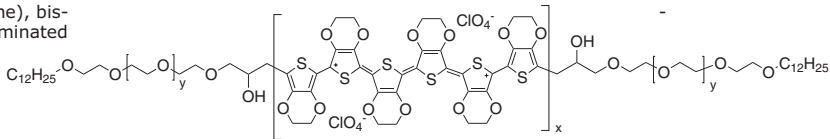
The transparent electrode, emissive material, and device architecture play an essential role in developing stretchable EL devices. Structure-enabled stretchable EL devices take advantage of well-developed EL devices and elastomeric interconnects for global stretchability. Efforts in this area center on designing innovative geometries to accommodate large strain while keeping the non-emissive area small. Conforming a buckled ultrathin EL layer on a pre-stretched elastomer substrate is a practical approach to large strains. The biggest challenge for intrinsically stretchable EL devices is integrating stretchable transparent electrodes and EL layers for high EL performance. Research shows that AgNWs, CNTs, doped conductive polymer, and ionic elastomer meet the surface conductivity, optical transparency, and stretchability requirements for the electrodes. Developing a stretchable EL (semiconductor) layer is still ongoing to achieve stretchable PLEDs and PLECs. Introducing stretchable microstructures to the otherwise unstretchable conjugated polymers appears to be a very promising approach. For ACEL devices, low bias, low alternating frequency, and high brightness are desired. Overall, PLEDs, PLECs, perovskite-polymer LEDs, and ACEL devices are all attractive candidates for stretchable EL devices and future stretchable displays. Further technical progress hinges on new material breakthroughs.

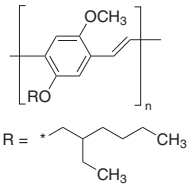

References

- (1) Gustafsson, G.; Cao, Y.; Treacy, G. M.; Klavetter, F.; Colaneri, N.; Heeger, A. J. *Nature* **1992**, *357* (6378), 477–479.
- (2) Chen, D.; Pei, Q. *Chem. Rev.* **2017**, *117* (17), 11239–11268.
- (3) Chen, Y.; Wu, Y.; Michael, S. S.; Carmichael, T. B. *Chem. Mater.* **2019**, *31* (6), 1920–1927.
- (4) Wang, Y.; Zhu, C.; Pfattner, R.; Yan, H.; Jin, L.; Chen, S.; Molina-Lopez, F.; Lissel, F.; Liu, J.; Rabiah, N. I.; Chen, Z.; Chung, J. W.; Linder, C.; Toney, M. F.; Murmann, B.; Bao, Z. *Sci. Adv.* **2017**, *3* (3), e1602076.
- (5) Yu, Z.; Niu, X.; Liu, Z.; Pei, Q. *Adv. Mater.* **2011**, *23* (34), 3989–3994.
- (6) Liang, J.; Li, L.; Niu, X.; Yu, Z.; Pei, Q. *Nat. Photonics* **2013**, *7* (10), 817–824.
- (7) Lipomi, D. J.; Lee, J. A.; Vosgueritchian, M.; Tee, B. C. K.; Bolander, J. A.; Bao, Z. *Chem. Mater.* **2012**, *24* (2), 373–382.

- (8) Bade, S. G. R.; Shan, X.; Hoang, P. T.; Li, J.; Geske, T.; Cai, L.; Pei, Q.; Wang, C.; Yu, Z. *Adv. Mater.* **2017**, *29* (23), 1607053.
- (9) Li, P.; Sun, K.; Ouyang, J. *ACS Appl. Mater. Interfaces* **2015**, *7* (33), 18415–18423.
- (10) Larson, C.; Peele, B.; Li, S.; Robinson, S.; Totaro, M.; Beccali, L.; Mazzolai, B.; Shepherd, R. *Science* **2016**, *351* (6277), 1071–1074.
- (11) Zheng, Y.; Wang, G. J. N.; Kang, J.; Nikolka, M.; Wu, H. C.; Tran, H.; Zhang, S.; Yan, H.; Chen, H.; Yuen, P. Y.; Mun, J.; Dauskardt, R. H.; McCulloch, I.; Tok, J. B. H.; Gu, X.; Bao, Z. *Adv. Funct. Mater.* **2019**, *29* (46), 1905340.
- (12) Liang, J.; Li, L.; Tong, K.; Ren, Z.; Hu, W.; Niu, X.; Chen, Y.; Pei, Q. *ACS Nano* **2014**, *8* (2), 1590–600.
- (13) Gao, H.; Chen, S.; Liang, J.; Pei, Q. *ACS Appl. Mater. Interfaces* **2016**, *8* (47), 32504–32511.
- (14) Kim, R. H.; Kim, D. H.; Xiao, J.; Kim, B. H.; Park, S. I.; Panilaitis, B.; Ghaffari, R.; Yao, J.; Li, M.; Liu, Z.; Malyarchuk, V.; Kim, D. G.; Le, A. P.; Nuzzo, R. G.; Kaplan, D. L.; Omenetto, F. G.; Huang, Y.; Kang, Z.; Rogers, J. A. *Nat Mater* **2010**, *9* (11), 929–37.
- (15) Hong, J.-H.; Shin, J. M.; Kim, G. M.; Joo, H.; Park, G. S.; Hwang, I. B.; Kim, M. W.; Park, W.-S.; Chu, H. Y.; Kim, S. J. *Soc. Inf. Display* **2017**, *25* (3), 194–199.
- (16) Li, Y. F.; Chou, S. Y.; Huang, P.; Xiao, C.; Liu, X.; Xie, Y.; Zhao, F.; Huang, Y.; Feng, J.; Zhong, H.; Sun, H. B.; Pei, Q. *Adv. Mater.* **2019**, *31* (22), e1807516.
- (17) Youssef, K.; Li, Y.; O’Keeffe, S.; Li, L.; Pei, Q. *Adv. Funct. Mater.* **2020**, *30* (33), 1909102.
- (18) Liu, J.; Wang, J.; Zhang, Z.; Molina-Lopez, F.; Wang, G.-J. N.; Schroeder, B. C.; Yan, X.; Zeng, Y.; Zhao, O.; Tran, H.; Lei, T.; Lu, Y.; Wang, Y.-X.; Tok, J. B. H.; Dauskardt, R.; Chung, J. W.; Yun, Y.; Bao, Z. *Nat. Commun.* **2020**, *11* (1).
- (19) Tan, Y. J.; Godaba, H.; Chen, G.; Tan, S. T. M.; Wan, G.; Li, G.; Lee, P. M.; Cai, Y.; Li, S.; Shepherd, R. F.; Ho, J. S.; Tee, B. C. K. *Nat. Mater.* **2020**, *19* (2), 182–188.

Electroluminescent Layer Products

Name	Structure	Purity/Mol Wt	Cat. No.
Diethyl 4-chlorobenzylphosphonate		97%	526061-10G
4-(Diphenylamino)phenylboronic acid		≥95%	647292-1G 647292-5G
8-Hydroxyquinoline zinc		99%	471755-5G
MDMO-PPV		$M_n \sim 120,000$	546461-250MG 546461-1G
Perylene		≥99.5%	394475-1G 394475-5G
Poly[9,9-bis-(2-ethylhexyl)-9H-fluorene-2,7-diyl]		-	571032-1G
Poly(9,9-di-n-hexylfluorenyl-2,7-diyl)		-	571040-1G
Poly(9,9-di-n-octylfluorenyl-2,7-diyl)		$M_w \geq 20000$	571652-500MG
Poly(3,4-ethylenedioxythiophene), bis-poly(ethyleneglycol), lauryl terminated		-	736287-25G

Name	Structure	Purity/Mol Wt	Cat. No.
Poly[2-methoxy-5-(2-ethylhexyloxy)-1,4-phenylenevinylene]		average M_n 40,000-70,000	541443-250MG 541443-1G
2,2',7,7'-Tetrabromo-9,9'-spirobifluorene		95%, HPLC	763888-1G 763888-5G

Carbon Nanomaterials

Name	Sheet Resistance (Ω /sq)	Cat. No.
Carbon nanotube sheet, aligned	resistivity 10-1000	901082-1EA
Carbon nanotube, single-walled, conductive aqueous ink	sheet resistance <600 (at 85% VLT (ohm/square), by 4-point probe on prepared film by rod coating)	791504-25ML 791504-100ML
Carbon nanotube, single-walled, solvent-based conductive ink, SWCNT	sheet resistance <1000 (by 4-point probe on prepared, at 87.5% VLT (ohm/sq))	792462-25ML 792462-100ML
Graphene, electrical conductivity $>10^3$ S/m	-	900561-500MG
Graphene dispersion	sheet resistance 4.8 k Ω /sq	900450-5ML 900450-20ML
Graphene nanoplatelets, Surfactant type: Anionic Surfactant	sheet resistance 10 (+/-5) (for a 25 μ m film)	799092-50ML

PEDOT:PSS Materials

Name	Sheet Resistance	Viscosity	Cat. No.
Graphene/PEDOT:PSS hybrid ink, dispersion in DMF	500 Ω /sq (20 nm film: 80% transmittance)	-	900442-50ML
Molybdenum trioxide/PEDOT:PSS ink, Solid content: 0.8 wt% crystalline MoO ₃ /PEDOT:PSS	-	6500s ⁻¹ shear rate at 25 °C	901047-10ML 901047-50ML
Poly(3,4-ethylenedioxythiophene)-poly(styrenesulfonate), Visual Light Transmission (VLT): \geq 80%	<200 Ω /sq (coating : 40 μ wet, drying: 6 min 130°C)	\leq 70 mPa.s at 20 °C	900181-100G
Poly(3,4-ethylenedioxythiophene)-poly(styrenesulfonate)	band gap 1.6 eV	-	483095-250G
Poly(3,4-ethylenedioxythiophene)-poly(styrenesulfonate)	500 Ω /sq (4 point probe measurement of dried coating based on initial 6 μ m wet thickness.) 500 Ω /sq (4 point probe measurement of dried coating based on initial 18 μ m wet thickness.)	10-30 cP at 20 °C	655201-5G 655201-25G
Poly(3,4-ethylenedioxythiophene)-poly(styrenesulfonate)	-	<20 cP at 20 °C	560596-25G 560596-100G
Poly(3,4-ethylenedioxythiophene)-poly(styrenesulfonate), neutral pH	<100 Ω /sq (>70% visible light transmission, 40 μ m wet)	<100 cP at 22 °C	739324-100G
Poly(3,4-ethylenedioxythiophene)-poly(styrenesulfonate), surfactant-free	<100 Ω /sq (<80% visible light transmission, 40 μ m wet)	30-100 cP at 20 °C	739332-100G
Poly(3,4-ethylenedioxythiophene)-poly(styrenesulfonate)	200-450 Ω /sq	-	768618-1G 768618-5G
Poly(3,4-ethylenedioxythiophene)-poly(styrenesulfonate), conductive screen printable ink	\leq 130 Ω /sq	\geq 50,000 mPa.s at 20 °C	768650-25G
Poly(3,4-ethylenedioxythiophene)-poly(styrenesulfonate), conductive inkjet ink	110 Ω /sq	7-12 cP at 22 °C	739316-25G
Poly(3,4-ethylenedioxythiophene)-poly(styrenesulfonate), dry re-dispersible pellets	<200 Ω /sq (by addition of 5% diethylene glycol)	-	900208-1G

Polyaniline Materials

Name	Mol. Wt.	Absorption	Cat. No.
High surface area conducting polyaniline	-	-	912891-2G
Polyaniline (emeraldine base)	~5,000	~325 nm	556459-5G 556459-25G
	~10,000	-	476706-10G 476706-50G
	~20,000	328 nm	556378-5G 556378-25G
	~50,000	~330 nm	556386-5G 556386-25G
	~65,000	331 nm	530689-10G 530689-50G
	~100,000	324 nm	576379-5G
Polyaniline (emeraldine salt)	>15,000	-	428329-5G 428329-25G
Polyaniline (emeraldine salt) short chain, grafted to lignin	-	-	561126-10G

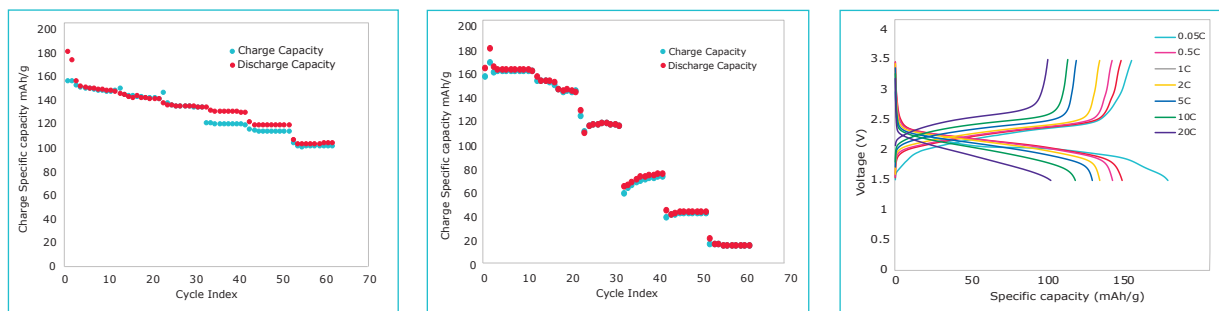
Polypyrrole Materials

Name	Form	Description	Cat. No.
High surface area conducting polypyrrole	solid	-	912573-2G
Polypyrrole	solid	coated on titanium dioxide doped	578177-10G
	solid	-	577030-5G 577030-25G
	solid	composite with carbon black doped	530573-25G
	solid	composite with carbon black undoped	577065-10G
	5 wt % dispersion in H ₂ O	doped	482552-100ML
	Polypyrrole-block-poly(caprolactone)	0.3-0.7 wt. % (dispersion in nitromethane), liquid (dispersion)	-

rGO Battery Electrode Materials

Fast Charge and Discharge Rates

Take advantage of the rate-enhancing capabilities of reduced graphene oxide in your battery research. Our methods transform a thorough mixture of redox polymers into well-dispersed reduced graphene oxide to create high-rate performance electrode materials for lithium-ion batteries.¹



A) Charge and discharge rate performance of PAQS/rGO composite electrode; B) Charge and discharge rate performance of PAQS electrode; C) Voltage profile of lithium metal half-cell battery with PAQS/rGO composite electrode at 0.5 to 20 C.

Green Batteries

Redox polymers are free of commonly used toxic transition metals such as cobalt and nickel used in lithium-ion batteries. This type of battery material also has the potential to be more sustainable.^{2,3}

Improved Capacity

Our reduced graphene oxide composites show a fourfold increase in capacity at 10 C compared to PAQS.

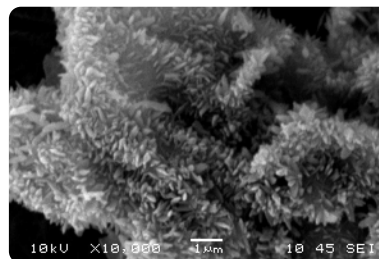


Figure 2: SEM image showing PMDA polymer coated on reduced graphene oxide.

Fast Charge/Discharge Li-Ion Battery Electrode Materials

Cat. No.	Product Description
921351	Reduced graphene oxide enhanced poly (anthraquinonyl sulfide) (PAQS) battery electrode
921378	Reduced graphene oxide enhanced pyromellitic dianhydride (PMDA) battery electrode
921386	Reduced graphene oxide enhanced 1,4,5,8-naphthalenetetracarboxylic dianhydride (NTCDA) battery electrode

References:

- [1] Song, Z.; Xu, T.; Gordin, M. L.; Jiang, Y.-B.; Bae, I.-T.; Xiao, Q.; Zhan, H.; Liu, J.; Wang, D. *Nano Lett.* **2012**, *12*, 2205. DOI: 10.1021/nl2039666
- [2] Song, Z.; Zhan, H.; Zhou, Y. *Angew. Chem. Int. Ed.* **2010**, *49*, 8444. DOI: 10.1002/anie.201002439
- [3] Muench, S.; Wild, A.; Friebe, C.; Häupler, B.; Janoschka, T.; Schubert, U. S. *Chem. Rev.* 2016, *116*, 9438. DOI: 10.1021/acs.chemrev.6b00070

Van der Waals Heterostructures Down to One Dimensional Level: Synthesis, Characterization, and Applications



Rong Xiang,^{*1} Qi Zhang,^{1,2} Taiki Inoue,^{1,3} Shigeo Maruyama^{*1}

¹ Department of Mechanical Engineering, The University of Tokyo, Tokyo 113-8656, Japan

² College of Materials & Environmental Engineering, Hangzhou Dianzi University, Hangzhou, 310018, P. R. China

³ Department of Applied Physics, Osaka University, Osaka 565-0871, Japan

* E-mail: xiangrong@photon.t.u-tokyo.ac.jp; maruyama@photon.t.u-tokyo.ac.jp

Introduction

Van der Waals heterostructures (vdWHs) are synthetic quantum systems composed of atomically thin layers. Traditional semiconducting heterostructures require components with similar crystal structures; this strict lattice matching becomes less critical in vdWHs due to the weak (van der Waals) interaction between two adjacent planes. Fabrication of these 2D vdWHs occurs via sequentially stacking (mechanical transfer) or direct growth (chemical/physical vapor deposition). Moreover, the features in vdWHs are decided not only by the constituents but also by the relative crystallographic alignment; their physical properties can be further controlled or improved through electrostatic gating and strain engineering.^{1,2} The emergence of two-dimensional (2D) layered materials ranging from graphene, hexagonal boron nitride (h-BN) to molybdenum disulfide (MoS₂) provide versatile fundamental building blocks for many new types of vdWHs. As the field of 2D materials expands, vdWHs exhibit many new potential applications in next-generation electronics and optoelectronics, such as memories, light-emitting diodes (LEDs), and photodetectors.

When a 2D material is wrapped into a cylinder, the resulting nanotube exhibits some exciting functionalities since it combines the characteristics of both 2D and 1D materials such as diameter-dependent bandgap in carbon nanotubes (CNTs). This provides opportunities to create radial heterostructures such as 1D vdWHs. For instance, cylindrical 2D materials are being explored as single-photon emitters in nanophotonic circuitry due to the strong edge state effect on

the optoelectronic properties. Crystalline MoS₂ layers coated on CNTs as a conductive backbone can be applied to battery electrodes because MoS₂ channels offer more active lithium-ion intercalation sites. 1D vdWHs are a burgeoning research field, and the recent achievements and development of on these hybrids are significant.

This review presents the most recent research activities on 1D vdWHs, including the candidate materials, the synthetic techniques, and characterization methods. The optoelectronic applications are discussed in detail for different constructions of the 1D vdWHs-based devices (FETs, sensors, LEDs, photovoltaic devices, and light detection). Some challenges and perspectives for future development and applications of 1D vdWHs are also proposed to conclude the review.

Potential van der Waals Materials

Both CNTs and graphene contain exceptional mechanical and electrical characteristics and are potential van der Waals materials. CNTs were first reported in 1991 by S. Iijima; CNTs include single-layered nanotubes, which are commonly referred to as single-walled carbon nanotubes (SWCNT). Graphene, an allotrope of carbon consisting of a single layer of atoms arranged in a two-dimensional honeycomb lattice, came onto the scene more recently than CNTs. In this case, a CNT can be thought of as a sheet of graphene (**Figure 1A**) rolled into a cylinder. Intrinsic graphene is a zero-band-gap semiconductor; however, CNT exhibits metallic or semiconducting behavior (0–2 eV), as



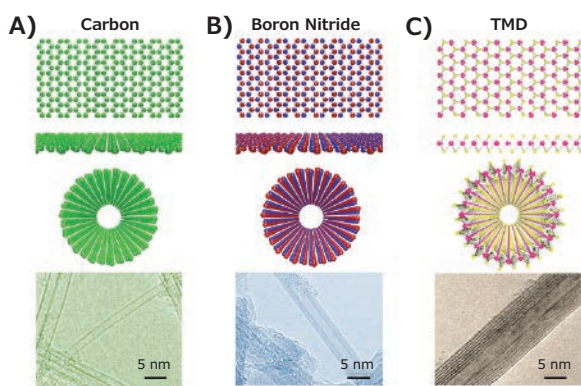


Figure 1. Crystal Structures of representative 2D van der Waals materials: **A)** carbon, **B)** boron nitride, **C)** MS_2 , where $M = Mo, W$, etc. and their corresponding tubular counterparts that have been experimentally evidenced.

determined by the rolling direction and radius (chirality). This striking modification of the electronic state by rolling into a tube with periodic boundary conditions made SWCNT a unique nanomaterial. Both show various applications in electronics, batteries, sensors, and more.⁴

The crystal texture of hexagonal boron nitride (h-BN, **Figure 1B**) is similar to graphite, where strong covalent bonds bind boron and nitrogen atoms in-plane, with adjacent layers coupled via van der Waals forces. Boron atoms lie over and above nitrogen atoms, responsible for the polarity of the B-N bonds. Boron nitride nanotubes (BNNTs), experimentally discovered in 1995, display electrically insulating properties with a bandgap of ~ 5.5 eV, independent of tube chirality and morphology. BNNTs have physicochemical features that allow for potential medical and biomedical applications, including gene delivery, drug delivery, and neutron capture therapy.

In 1992 discovery of transition metal dichalcogenide (TMD) nanotubes, like MoS_2 (**Figure 1C**), stimulated intense experimental and theoretical research of other fascinating inorganic tubular structures. Many TMDs are semiconductors (with tunable band-gaps from ~ 1 -2 eV, depending on the layer thickness), and research on 2D TMDs, demonstrates a transition from indirect band-gap to direct band-gap when the thickness reduces to a monolayer.³ All these unique features, combined with appreciable charge mobility, make TMD materials promising candidates for high-performance optoelectronics.¹

Synthesis and Assembly Techniques

CNTs and BNNTs are produced via well-established techniques, including arc-discharge, laser ablation, and chemical vapor deposition. But there were only a few reports on the successful production of other tubular structures (e.g., TMDs) using these synthetic approaches. An alternative route has focused on using a tubular template such as a CNT to facilitate atom packing:

Figure 2A presents a solvothermal process to realize the 1D vdWHs. Here, amorphous MoS_2 sheath wrapped around the CNT

serves as an intermediate coating on CNTs and allows conversion into crystalline sheets upon thermal annealing. Removal of residual particles that can lead to scattering of electrons and photons is required when using the precursors in the solution method. When using a solvent-free high-temperature route, experiments have produced SWCNT@BNNT, SWCNT@ MoS_2 NT, and even a ternary SWNT@BNNT@ MoS_2 NT (**Figure 2B**). Each layer shows single-crystalline nature, and different van der Waals cylinders are coaxially nested, confirming an open-end growth mechanism contributes to the formation process.⁴ For these as-prepared vdWHs, the active materials or the target nanotube sits outside the template, exposed to a foreign environment, where some materials may be unstable or even become damaged. As a result, efforts are also focussed on confining the formation of the second phase to the tubular template. In previous dry or wet methods, the nanotube ends must remain open, and a long-term thermal annealing process is required to facilitate precursor penetration. Tobias and colleges presented a laser-assisted strategy (**Figure 2C**) for cylindrical vdWHs, allowing the encapsulation of single-layered lead iodide into the cavities of CNTs. More importantly, the carbon shell protected the air-sensitive lead iodide, and the cylindrical vdWHs were able to be directly manipulated under ambient conditions.

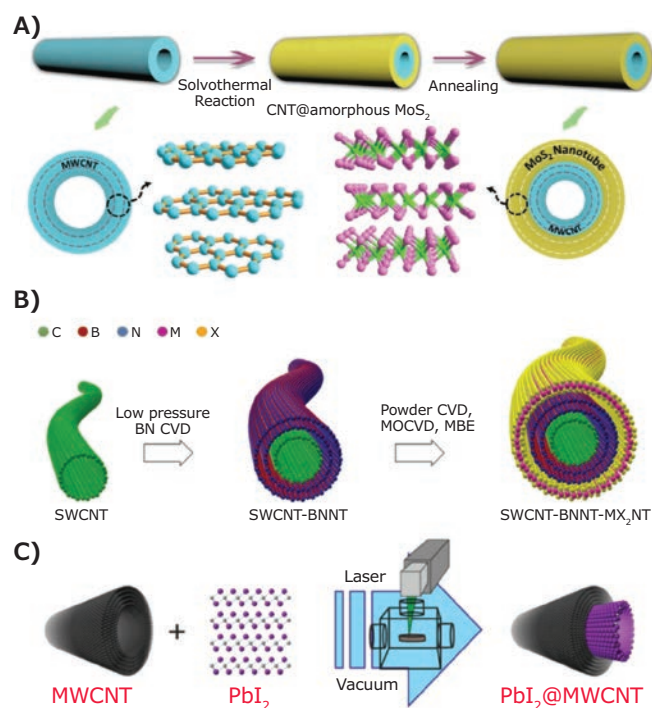


Figure 2. **A)** Schematic representation of the solvothermal synthesis process of coating crystalline MoS_2 layers onto CNTs. Reprinted with permission from reference 9, copyright 2016 WILEY-VCH Verlag GmbH & Co. KGaA, Weinheim. **B)** Sketch shows the solvent-free high-temperature route of a SWCNT-BNNT- MX_2 NT 1D vdWHs. Reprinted with permission from reference 4, copyright 2021 American Association for the Advancement of Science. **C)** Illustration of the laser-assisted filling of multiwalled carbon nanotubes. Reprinted with permission from reference 12, copyright 2018 American Chemical Society.

Characterization of 1D vdWHs

Obtaining the structural information of 1D vdWHs, is essential, particularly near the interface, this is primarily obtained through high-resolution transmission electron microscopy (HRTEM) typically by employing spherical aberration correction. In a typical HRTEM image (Figure 3A), PbI_2 layers are conformably encapsulated in the inner core of the host WS_2 nanotubes (Figure 3B). The two phases can be distinguished via different layer distances (Figure 3C).¹⁵ Electron microscopy with adjustable irradiation offers a powerful tool to uncover the growth dynamics of the 1D vdWHs, i.e., the formation of a PbI_2 nanotube in such a confined geometry (Figure 3D), where a continuous blending of the nanorod onto the nanotube has been directly evidenced.

The optoelectronic properties of 1D vdWHs can be modulated because carriers (holes and electrons) in the atomically thin layers are exposed to layer-to-layer coupling.¹ The absorption spectrum of BNNT@SWCNT (in Figure 3E) presents a new peak emerging at 6.1 eV compared to that of pristine CNTs,

associated with π - π^* bands of the BNNTs. Meanwhile, a blue-shift (5–10 cm^{-1}) of the G band (relative to CNT) has been demonstrated in the BNNT@SWCNT vdWHs, using Raman characterization (Figure 3F); a possible explanation for this shift is the thermal strain between BNNT and CNT.⁴ As to the X-ray photoelectron spectroscopy (XPS) spectrum of MoS_2 @CNT vdWHs (Figure 3G), a downshift of the C 1s line by 0.15 eV appears as compared with the pristine CNTs, attributed to a decrease in the Fermi level energy led by the p-doping of CNTs. Although not fully documented yet, there should be strong electronic and excitonic coupling between different nanotubes in a 1D vdWH. The precise understanding of the characterization and evaluation of those vdWHs is significant for their further applications once their dimension is down to 1 nm.

Potential Applications

Semiconductor heterostructures are considered the base of modern optoelectronics, specifically for LEDs and solar cells.² 1D vdWHs with radially modulated compositions/band-gaps provide a platform for a deep understanding of the hetero interface

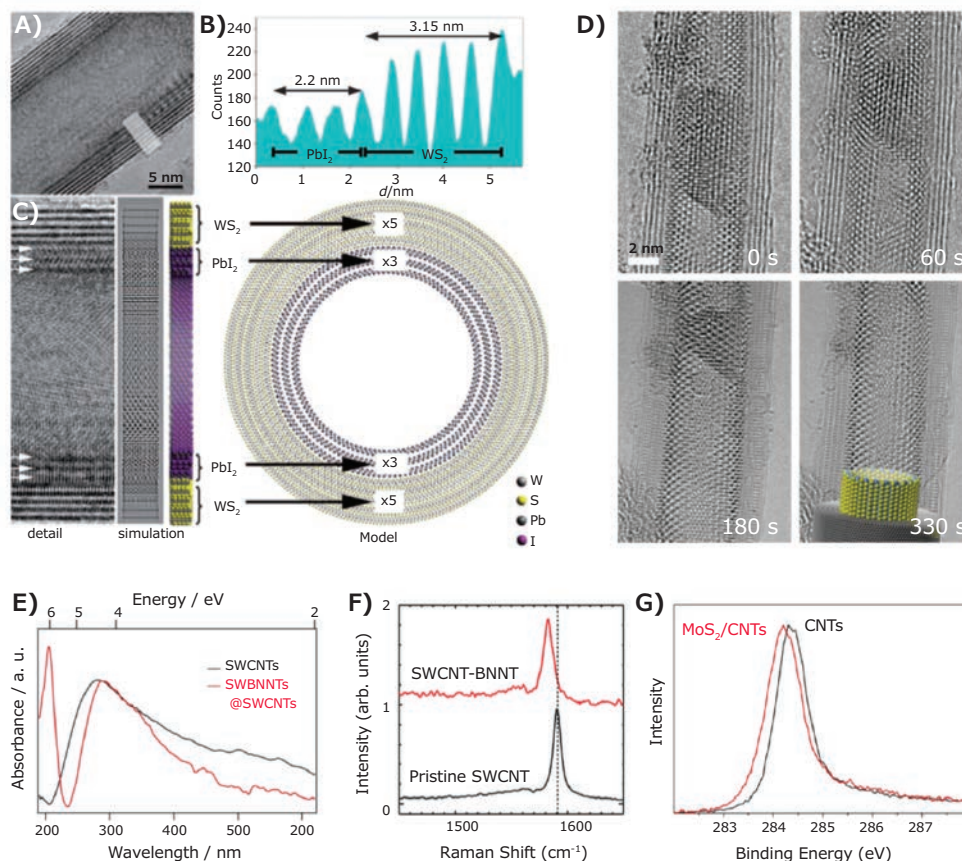


Figure 3. A) HRTEM micrograph showing a core-shell PbI_2 @ WS_2 composite nanotube. B) Line profile obtained from the indicated region in-plane (A); C) the complex contrast of the inner PbI_2 layers (arrowed) relative to the outer WS_2 layers. Reprinted with permission from reference 13, copyright 2016 Wiley-VCH Verlag GmbH & Co. KGaA, Weinheim. D) Sequence of images showing the transformation from a nanorod fragment onto a single-layered nanotube, cyan, green and grey spheres representing Pb, I and C atoms, respectively. Reprinted with permission from reference 14, copyright 2016 WILEY-VCH Verlag GmbH & Co. KGaA, Weinheim. E) Absorption spectroscopy of SWCNTs and SWBNNT@SWCNTs. Reprinted with permission from reference 15, copyright 2016 Springer Nature. F) Raman presents typical G band of an individual SWCNT before and after BN coating. Reprinted with permission from reference 4, copyright 2021 American Association for the Advancement of Science. G) XPS C 1s spectra of pristine CNT sample and MoS_2 /CNTs composite. Reprinted with permission from reference 16, copyright 2011 American Chemical Society.

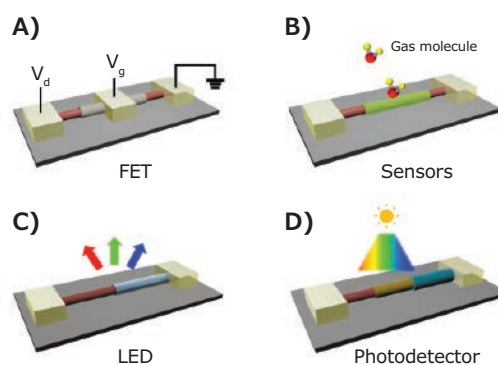


Figure 4. Schematic diagrams of a device using the 1D vdWHs: **A)** a “gate-all-around” field-effect transistor, **B)** a chemical or biological sensor, **C)** LED, **D)** broadband spectrum photodetector.

and have shown great potential for various semiconductor systems, such as high mobility transistors, chemical sensors, photodetectors, and photovoltaic cells.^{11,14} The reduced dimension of the vdWHs (down to 1D level) creates challenges for manipulating these samples during device fabrication. Here, we briefly discuss the 1D vdWH-based optoelectronic devices available currently or in the near future.

First, we will examine field-effect transistors (FETs), schematically illustrated in **Figure 4A**, where the conductive channel (CNT) can be completely isolated by the dielectric layer (BNNT). High mobility is expected because the free surface dangling bonds lead to a significant carrier scattering reduction,³ but an appropriately thick dielectric layer is required to prevent gate leakage.¹² In addition, the high thermal stability of both SWCNT and BNNT, makes these transistors appealing for creating durable commercial integrated circuits.

Chemical sensors based on 2D vdWHs for detecting various gases, such as nitrogen dioxide (NO_2) and ammonia (NH_3), rely on the capture/release of free electrons at the semiconductor surface.² This is also the base principle for 1D vdWHs (**Figure 4B**). Once exposed to the target gas molecules (e.g., NO_2), the change in carrier density of the outer shell (MoS_2) modulates the transport in the core channel (e.g., CNT) via the surface gating effect. Due to the large interfacial area, sensitivity as low as ppm level may be achieved, vital for environmental monitoring systems.

The core-shell geometry enables a low recombination rate and a high efficiency of charge collection, principally attributed to shortened migration paths for the minority carriers. This makes coaxial junctions established on type-II band alignment, like P-N or metal-insulator-semiconductor heterojunctions (e.g., p-CNT/BNNT/n- MoS_2), practical for high-efficiency light-emitting (**Figure 4C**) or photovoltaic devices. Note that careful energy band matching is required since the band gap of SWCNT strongly depends on its chirality. In cylindrical heterostructures like these, a strong polarization dependence may be observed due to crystal anisotropy one interesting result is that LEDs based on 1D vdWHs could be used for integrated optoelectronics due to their small diameters.

The vdWHs discussed here provide more tunability for band alignments and carrier densities and have shown promising applications in high-performance photodetectors. Previous work has shown that position control of the heterojunctions within an individual tube (with different optical band gaps), opens the door for multispectral or broadband sensing (**Figure 4D**).¹² This makes possible an entire spectroscopy system within an individual tubular structure, rendering a path to miniaturized spectroscopic applications.

Challenges, Outlook, or Prospect

VdWHs based on low-dimensional materials have seen significant development in recent years due to their strong localized states at the submicron scale. Here, we present a brief review of 1D vdWHs, including the candidate materials, synthetic routes,

characterization methods, and potential applications, including transistors, chemical sensors, LEDs, and photovoltaic devices photodetectors. However, compared with the 2D vdWHs, 1D vdWHs have yet to attract significant attention, although research is beginning to show their significant potential for next-generation integrated circuits. The controllable preparation of 1D vdWHs is indispensable. Sub-mm-large 2D vdWHs can be obtained either by transfer or direct growth. Fabrication of long and perfect coaxial junctions will be imperative for advancing new studies. While the CVD method can grow high-quality single crystals, there is still a technical challenge to preparing ultralong 1D vdWHs due to low efficiency of the gas-feeding-dominant process. At the current stage, high growth temperate (>1000 °C) and the vacuum environment hinder industrial production. Further work should balance the reaction temperature and the growth efficiency; a catalytic assisted route may be feasible. Second, the number of materials appropriate for 1D vdWHs (mainly CNT, BNNT, and MoS_2) is too few compared to 2D vdWHs. The rising PbI_2 indicates a possible supplement. Another challenge is the precise control of inner and outer atomic arrangements, and chirality or polarity in a tubular structure. It may be interesting to fabricate 1D vdWHs using chirality-free templates. The decrease in 1D vdWHs' dimension (less than 1 nm) may also requires new theoretical work given the strong quantum effect and the inter-tube coupling. In summary, 1D vdWHs are an essential conceptual novelty in the materials community and only the persistent exploration of 1D vdWHs will fulfill their promising application in next-generation optoelectronics.



Acknowledgments

RX, QZ contributed equally to this work. Part of this work was supported by JSPS KAKENHI (grant numbers JP18H05329, JP19H02543, JP20H00220, 20K14660, and JP20KK0114) and by JST, CREST grant number JPMJCR20B5, Japan. Part of the work was conducted at the Advanced Characterization Nanotechnology Platform of the University of Tokyo, supported by the “Nanotechnology Platform” of the MEXT, Japan, grant number JPMXP09A20UT0063.

References

- Rhodes, D.; Chae, S. H.; Ribeiro-Palau, R.; Hone, J. *Nat. Mater.* **2019**, *18*, 541–549.
- Yu, J. D.; Wang, L.; Hao, Z. B.; Luo, Y.; Sun, C. Z.; Wang, J.; Han, Y. J.; Xiong, B.; Li, H. T. *Adv. Mater.* **2020**, *32*, 1903407.
- Novoselov, K. S.; Mishchenko, A.; Carvalho, A.; Castro Neto, A. H. *Science* **2016**, *353*, aac9439.
- Xiang, R.; Inoue, T.; Zheng, Y. J.; Kumamoto, A.; Qian, Y.; Sato, Y.; Liu, M.; Tang, D. M.; Gokhale, D.; Guo, J.; Hisama, K.; Yotsumoto, S.; Ogamoto, T.; Arai, H.; Kobayashi, Y.; Zhang, H.; Hou, B.; Anisimov, A.; Maruyama, M.; Miyata, Y.; Okada, S.; Chiashi, S.; Li, Y.; Kong, J.; Kauppinen, E. I.; Ikuhara, Y.; Suenaga, K.; Maruyama, S. *Science* **2020**, *367*, 537–542.
- Soto Lamata, I.; Alonso-González, P.; Hillenbrand, R.; Nikitin, A. Y. *ACS Photonics* **2015**, *2*, 280–286.
- Bindumadhavan, K.; Srivastava, S. K.; Mahanty, S. M. *Chem. Commun.* **2013**, *49*, 1823–1825.
- Iijima, S. *Nature* **1991**, *354*, 56.
- Chopra, N. G.; Luyken, R. J.; Cherrey, K.; Crespi, V. H.; Cohen, M. L.; Louie, S. G.; Zettl, A. *Science* **1995**, *269*, 966–967.
- Wang, Y. S.; Ma, Z. M.; Chen, Y. J.; Zou, M. C.; Yousaf, M.; Yang, Y. B.; Yang, L. S.; Cao, A. Y.; Han, R. P. S. *Adv. Mater.* **2016**, *28*, 10175–10181.
- Xiang, R.; Maruyama, S. *Small Sci.* **2021**, *1* (2), 2000039.
- Walker, K. E.; Rance, G. A.; Pekker, A.; Tohati, H. M.; Fay, M. W.; Lodge, R. W.; Stoppiello, C. T.; Kamaras, K.; Khlobystov, A. N.; *Small Methods* **2017**, *1*, 1700184.
- Sandoval, S.; Kepic, D.; del Pino, A. P.; Gyorgy, E.; Gomez, A.; Pfannmoeller, M.; Van Tendeloo, G.; Ballesteros, B.; Tobias G. *ACS Nano* **2018**, *12*, 6648–6656.
- Kreizman, R.; Hong, S. Y.; Sloan, J.; Popovitz-Biro, R.; Albu-Yaron, A.; Tobias, G.; Ballesteros, B.; Davis, B. G.; Green, M. L. H.; Tenne, R. *Angew. Chem.* **2009**, *121*, 1256–1259.
- Cabana, L.; Ballesteros, B.; Batista, E.; Magen, C.; Arenal, R.; Oro-Sole, J.; Rurali, R.; Tobias, G. *Adv. Mater.* **2014**, *26*, 2016–2021.
- Nakanishi, R.; Kitaura, R.; Warner, J. H.; Yamamoto, Y.; Arai, S.; Miyata, Y.; Shinohara, H. *Sci. Rep.* **2013**, *3*, 1385.
- Koroteev, V. O.; Bulusheva, L. G.; Asanov, I. P.; Shlyakhova, E. V.; Vyalikh, D. V.; Okotrub, A. V. *J. Phys. Chem. C* **2011**, *115*, 21199–21204.
- Feng, Y.; Li, H.; Inoue, T.; Chiashi, S.; Rotkin, S. V.; Xiang, R.; Maruyama, S. *ACS Nano* **2021**, *15* (3), 5600–5609.
- Tang, J. Y.; Huo, Z. Y.; Brittan, S.; Gao, H. W.; Yang, P. D. *Nat. Nanotechnol.* **2011**, *6*, 568–572.
- Yang, Z. Y.; Albrow-Owen, T.; Cui, H. X.; Alexander-Webber, J.; Gu, F. X.; Wang, X. M.; Wu, T. C.; Zhuge, M. H.; Williams, C.; Wang, P.; Zayats, A. V.; Cai, W. W.; Dai, L.; Hofmann, S.; Overend, M.; Tong, L. M.; Yang, Q.; Sun, Z. P.; Hasan, T. *Science* **2019**, *365*, 1017–1020.
- Liu, M.; Hisama, K.; Zheng, Y.; Maruyama, M.; Seo, S.; Anisimov, A.; Inoue, T.; Kauppinen, E. I.; Okada, S.; Chiashi, S.; Xiang, R.; Maruyama, S. *ACS Nano* **2021**, *15* (5), 8418–8426.

Fullerene

Structure	Name	Purity (%)	Cat. No.
	Fullerene-C ₆₀	99.9	572500-250MG 572500-1G 572500-5G
	Fullerene-C ₇₆	98	482951-5MG

Single-Walled Carbon Nanotubes

Name	Carbon Content (%)	Dimensions	Origin Of Nanomaterial	Cat. No.
Carbon nanotube, single-walled	≥95% carbon basis (≥95% as carbon nanotubes)	-	CoMoCAT™ Catalytic Chemical Vapor Deposition (CVD) Method	773735-250MG 773735-1G
	2% (Metallic) 98% (Semiconducting)	L 0.3-5 μm	Electric Arc Discharge Method	750522-1MG
Carbon nanotube, single-walled, carboxylic acid functionalized	>90% carbon basis	D × L 4-5 nm × 0.5-1.5 μm (bundle dimensions)	Electric Arc Discharge Method	652490-250MG 652490-1G
Carbon nanotube, single-walled	≥90% carbon basis (≥77% as carbon nanotubes)	-	CoMoCAT™ Catalytic Chemical Vapor Deposition (CVD) Method	704121-250MG 704121-1G

Monolayer Graphene

Name	Description	Cat. No.
Easy transfer monolayer graphene	-	GRTRANSFER25-1EA
Monolayer graphene film	1 in x 1 in on PET film	745863-1EA 745863-5EA
	2 in x 2 in on PET film	745871-1EA
	R2R Monolayer large grain CVD graphene on copper foil	A3 size Growth method: roll-to-roll CVD Number of layer: Monolayer Raman intensity 2D/G: ≥1.5
	A5 size Growth method: roll-to-roll CVD Raman intensity 2D/G: ≥1.5 Number of layer: Monolayer	920088-1EA

Name	Description	Cat. No.
R2R Monolayer large grain CVD graphene on silicon wafer	4 in diameter Growth method: roll-to-roll CVD Wafer: SiO ₂ (300nm) Si Number of layer: Monolayer Raman intensity 2D/G: ≥1.5	920126-1EA
	6 in diameter Growth method: roll-to-roll CVD Wafer: SiO ₂ (300nm) Si Number of layer: Monolayer Raman intensity 2D/G: ≥1.5	920134-1EA
R2R Monolayer small grain CVD graphene on copper foil	A3 size Growth method: roll-to-roll CVD Number of layer: Monolayer Raman intensity 2D/G: ≥1.5	920061-1EA
	A5 size Growth method: roll-to-roll CVD Number of layer: Monolayer Raman intensity 2D/G: ≥1.5	920096-1EA
R2R Monolayer small grain CVD graphene on silicon wafer	4 in diameter Growth method: roll-to-roll CVD Wafer: SiO ₂ (300nm) Si Number of layer: Monolayer Raman intensity 2D/G: ≥1.5	920118-1EA

MAX-Phase Materials

Name	Form	Particle Size (µm)	Purity	Cat. No.
Titanium aluminium carbide 211	powder	≤40	≥80%	910759-25G
	powder	≤100	≥80%	910821-25G
	powder	≤200	≥80%	910708-25G
Titanium aluminium carbide 312	powder	≤40	≥90%	910775-25G
	powder	≤100	≥90%	910767-25G

Hexagonal Boron Nitride

Name	Description	Cat. No.
Hexagonal boron nitride ink	Solid content : 20-40% for blade coating	901349-10ML
	Solid content : 4.4-6.4% for inkjet printing	901410-5ML

FlexAbility!

Our wide range of printed electronic products, from inks to substrates, enable your creation to come alive. We offer printable inks at various viscosities and particle size, and flexible/rigid substrates with various sizes and thicknesses.

- Conductive Inks
- Semiconductor Inks
- Dielectric Inks
- Substrates

Explore our full product list, please visit
SigmaAldrich.com/PrintedElectronics



MilliporeSigma is the U.S. and Canada Life Science business of Merck KGaA, Darmstadt, Germany.

Sigma-Aldrich®
Lab & Production Materials



High Crystalline, Solution-processable Organic Field-Effect Transistors



Zhenfei He, Ming Chen, Paddy Kwok Leung Chan*

Mechanical Engineering Department, The University of Hong Kong, Hong Kong
* Email: pklc@hku.hk

Background and Introduction

Flexible transistors are the building blocks of next-generation soft electronics. Among all the reported material systems that can be fabricated by researchers, such as circuits, biosensors, stretchable displays, and others,¹⁻⁵ small molecular weight organic semiconductors are among the most promising candidates for flexible transistor applications. For these small molecular weight organic semiconductors, the semiconductor forming the conductive channel dominates the device performance. Unlike inorganic counterparts like silicon or metal dichalcogenides with strong intermolecular bonding, these small molecules, although they can be packed exceptionally well under certain conditions, are usually held together by the weak van der Waals force only. As a result, the organic semiconductors in thin-film structures have better flexibility than inorganic semiconductors. The drawback, however, is the weaker carrier transport efficiency. Other than flexibility, another significant advantage of organic semiconductors is their tunability. Chemical or electrical properties like π - π stacking,⁶ responsivity to light with different wavelengths,^{7,8} and solubility in solvents⁹ can be adjusted by modifying the structure of the organic molecules or adding extra functional groups. As a result, one can tailor-make the molecules they want for specific applications, bringing organic transistors to a much broader spectrum of applications.

To date, thermal evaporation and solution processing dominate the fabrication of thin-film small molecule organic field-effect transistors (OFETs). As one of the commonly adapted vapor phase depositions, thermal evaporation is very suitable for large-area processing. However, thermal evaporated organic thin films typically have a polycrystalline structure with randomly orientated grains in varied sizes. density

The distribution of grains varies significantly among devices even when on the same substrate. The presence of the grain boundaries and the grain misalignment reduces the carrier mobility of the OFETs. Solution processing includes different methods like spin coating and ink-jet printing each with advantages and disadvantages. Spin coating is a fast technique and excellent for testing the intrinsic transport properties of the thin film; however, uniformity and compatibility with patterning can be a concern. Direct patterning is straightforward in ink-jet printing. However, similar to thermal evaporation, the weak control of the grain orientations is a common disadvantage of both approaches.

To address the orientation problem and guide the molecules, researchers developed a low-speed solution shearing method using the meniscus line to guide the deposition of organic molecules. In this method, the organic molecules "line up" at the meniscus before deposition onto the substrate. As a result, the crystal grows gradually in a direction parallel to the meniscus line and the size of the crystals is orders of magnitude larger than that developed by spin coating or ink-jet printing. Herein, we discuss a solution shearing method to achieve high-performance OFETs and their resulting performance.

Causes of Variations Among Devices

Device-to-device variation and reproducibility are crucial bottlenecks in the development of OFETs. Due to the quality of the organic thin film, the metal-organic interface or dielectric-organic interfaces are susceptible to processing parameters like deposition rate, deposition environment, or substrate surface quality. Thus, even when materials and fabrication equipment



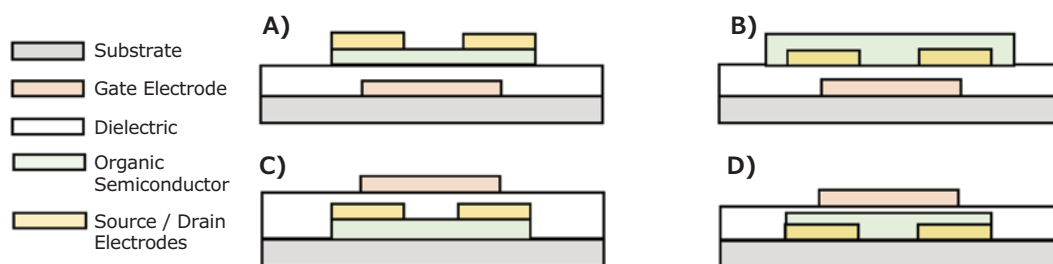


Figure 1. The four standard structures of OFET. **A)** Bottom gate top contact. **B)** Bottom gate bottom contact. **C)** Top gate top contact, and **D)** Top gate bottom contact. (A) and (D) are also known as staggered structures, while (B) and (C) are known as coplanar structures.

remain the same, the performance of OFETs from different groups can still vary significantly. Standardized substrates with the same quality predeveloped dielectric and electrodes on it are highly desired (Cat. No. **FIPMS176**, **FIPMS148**, **FIPMS223**, **FIPMS175**). The bottom gate, bottom contact (coplanar) OFETs can be finished by spin-coating or blade-coating the active layer directly onto the substrate. It is important to note that metal deposition onto organic semiconductors can be a rather sensitive process. Unlike the bottom contact devices, the quality of the metal-organic interface in the top contact OFETs strongly depends on the penetration depth of the metal atoms in the organic thin film. This penetration depth is related to the thickness of the semiconductor, the deposition rate, the packing density of the organic thin-film, as well as other factors. The effect of metal atom penetration is particularly critical when the bottom semiconductor layer is only a monolayer or a few layers thick. Although the coplanar structure OFETs may suffer from higher contact resistance, it does not have the same penetration depth issue as the staggered OFETs.

Different Structures of Solution Shearing OFETs

A schematic diagram of OFETs with the bottom gate top and bottom contact configuration is shown in **Figures 1A** and **B**, respectively. In the bottom gate configuration, the active layers are coated on the surface of the dielectrics, which play a vital role in device performance. The bottom gate structure is commonly adopted because a uniform, smooth substrate is favourable for semiconductor growth. A silicon substrate (Si) with silicon dioxide (SiO_2) provides a good substrate for semiconductor thin film growth,¹⁰⁻¹⁴ with a mobility exceeding $10 \text{ cm}^2\text{V}^{-1}\text{s}^{-1}$ can be achieved in a Si/ SiO_2 substrate-based OFET. To further improve the crystallinity of solution sheared organic thin films, several modifications to the application process are possible, such as a micropillar patterned blade to induce the recirculation of the solution,¹⁵ screen printing with polymer banks,¹⁶ blending solvents with induced Marangoni flow,¹³ or use of ion liquid hosted in porous anodized aluminium oxide as a substrate.¹⁷ The effect of the dielectric/semiconductor interface on the OFET is a popular research direction towards higher performance OFETs.

Other than improving carrier mobility, recent advances in solution sheared OFETs also include optimizing the operating voltage. A lower operating voltage can be beneficial for portable or wearable applications. Kitahara et al. reported a meniscus-controlled printing approach in which organic semiconductor thin films are blade coated on the surface of CYTOP™ with negligible traps, and realizing a subthreshold swing (SS) of 63 mV dec^{-1} . This reveals the extremely sharp switching property of a transistor.¹⁸ A small SS value implies the device can be switched from off-state to on-state with a low voltage supply. A dielectric with high dielectric constants is also commonly used to reduce the operating voltages of the OFETs and suppress the short channel effect.^{12,19} Size miniaturization is essential on the path towards high-frequency operation.^{12,20} One drawback of the bottom gate top contact (BGTC) structure is the potential for thermal damage to the organic semiconductor during electrode deposition. The bottom gate bottom contact (BGBC, **Figure 1B**) structure can eliminate this potential damage and achieve highly reproducible results.²¹ Thus, this structure is very suitable for the quick screening of the intrinsic semiconductor properties without worrying about the device variation induced by the source and drain electrodes.

Besides the bottom gate configuration, the top gate (TG) structure (**Figure 1C–D**) is highly desired for independent gate control and adapted for driving circuits in a display application. In this structure, the dielectric insulator can also serve as the encapsulation layer to protect the channel from the surrounding environment. However, the compatibility of the dielectric layer deposition and the bottom organic thin film needs to be adjusted for this configuration. The processing temperature or the solvent used to develop the dielectric materials also need to induce a negligible effect on the organic semiconductor channel.^{22,23}

State of the Art Performance of Solution Shearing Devices

In the operation of the OFETs, one indicator of device quality is operating frequency. The cutoff frequency (f_T) of OFET is the frequency at which the transistor loses the amplifier ability. The cut off frequency is given as,²⁴

$$f_T = \frac{\mu_{\text{eff}}(V_G - V_{th})}{2\pi L(\frac{2}{3}L + 2L_C)}$$

where μ_{eff} is the effective mobility, V_G is the applied gate voltage, V_{th} is the threshold voltage, L is the channel length, and L_C is the contact length. As shown in the equation, a short channel and high effective mobility would be beneficial to achieve fast-speed operation. Borchert et al. and Yamamura et al. fabricated a transistor operating at 21 MHz²⁵ and 29 MHz²⁶, respectively, by using a short channel down to a few micrometers or even sub micrometers, based on 2,9-diphenyl-dinaphtho-[2,3-b:2',3'-f]thieno[3,2-b]thiophene (DPh-DNTT) and 3,11-dioctyldinaphtho[2,3-d:2',3'-d']benzo[1,2-b:4,5-b']dithiophene (C_8 -DNBDT-NW). For mobility, Peng et al. demonstrated a highly crystalline monolayer 2,9-didecyl-dinaphtho[2,3-b:2',3'-f]thieno[3,2-b]thiophene (C_{10} -DNTT) OFET with the mobility of $10.4 \text{ cm}^2\text{V}^{-1}\text{s}^{-1}$ by dual solution shearing method (Figure 2A).²⁷ Kumagai et al. used meniscus guided coating to fabricate a 4-inch wafer size 3,11-dinonyldinaphtho[2,3-d:2',3'-d']benzo[1,2-b:4,5-b']dithiophene (C_9 -DNBDT-NW) single crystal by continuous edge casting method (Figure 2B).²⁸ The OFETs showed high reproducibility with the mobility of $10 \text{ cm}^2\text{V}^{-1}\text{s}^{-1}$ and an on-off ratio in the order of 10^7 . Besides blade coating, a water-surface drag coating method, as illustrated in Figure 2C, has also been employed to develop a single-crystal thin film of 2,8-difluoro-5,11-bis(triethylsilylethynyl)anthradithiophene (DiF-TES-ADT).²⁹ In this method, the organic molecules spread with the help of water surface tension, keeping them free from external force and

enabling self-assembly into a highly crystalline film. The mobility of DiF-TES-ADT/polymer polystyrene (PS) blended OFET devices showed 5 times improvement compared with the blade-coating method and exhibited mobility of $10.1 \text{ cm}^2\text{V}^{-1}\text{s}^{-1}$.

The potential to control the thickness of the organic thin-film down to the monolayer is another attractive aspect of the solution shearing method, which can minimize the short channel effect when scaling down the channel dimensions as a thin or monolayer channel.¹⁹ The access resistance (R_{acc}) component in the contact resistance (R_c) can also be minimized by the monolayer channel. Previously, a monolayer C_{10} -DNTT single crystal has been demonstrated by solution shearing, attaining a width normalized contact resistance as low as $40 \text{ W}\cdot\text{cm}$.¹¹ Besides R_{acc} , the other component in the contact resistance is the interface resistance (R_{int}) between the metal electrode and the organic semiconductor. The R_{int} exists because of the mismatch of the work function of metal and organic semiconductors (OSC) energy levels. Yamamura et al. addressed this by inserting a dopant layer of 2,3,5,6-tetrafluoro-7,7,8,8-tetracyanoquinodimethane (F_4 -TCNQ, Cat. No. 376779) or 1,3,4,5,7,8-hexafluoro-tetracyanonaphthoquinodimethane (F_6 -TNAP) between the metal/OSC (C_9 -DNBDT-NW) interface.³⁰

Another critical parameter in the operation of an OFET is the SS. It describes the amount of supply voltage that could increase the current value of one order near the transistor

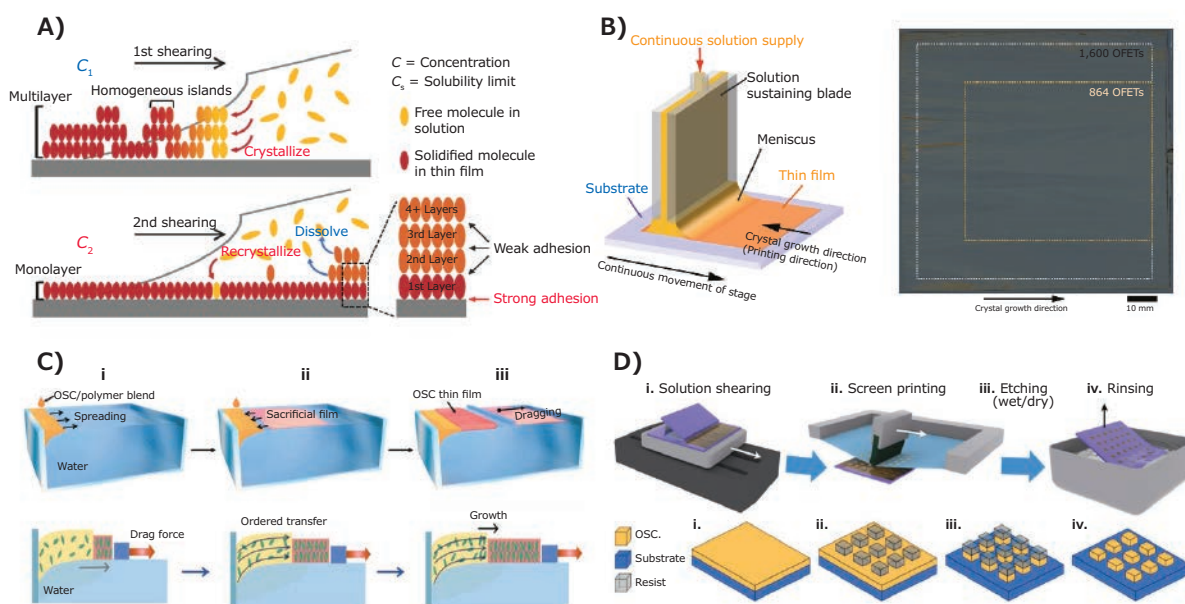


Figure 2. Shearing methods for high crystalline film deposition. **A)** Dual solution shearing method. Multilayer crystals with different orientations were formed at the 1st shearing. At the 2nd shearing, the upper layers were dissolved because of weak interlayer adhesion, while the bottom monolayer crystal was dissolved slowly and recrystallized due to strong adhesion to the substrate, leaving the high-crystalline monolayer. Reprinted with permission from reference 27, copyright 2017 Wiley. **B)** Continuous edge casting method. Crystal nanosheet was formed at the vapor-liquid interface of the meniscus line, where the solution is supersaturated because of solvent evaporation. The nanosheet was laminated on the substrate with the substrate movement. 1600 OFETs were fabricated on a 4-inch size wafer. Reprinted with permission from reference 28, copyright 2019 Nature. **C)** Water-surface drag coating method. A discrete OSC/PS film was used as the sacrificial film to control solvent spread. The triggered the spread of solution by dragging at the contact line pushed the nuclei to move. At the same time, with the solvent evaporation at the contact line, a crystal was gradually grown. Reprinted with permission from reference 29, copyright 2019 Wiley. **D)** Simple solution shearing method and semiconductor patterning method by the resist. Water-soluble resist was printed onto crystal films. And then unprotected layer was etched by organic solvent /oxygen plasma. Last, the resist was removed by ultrapure water. Reprinted with permission from reference 35, copyright 2020 Wiley.

turn-on regime. Besides low voltage consumption, a small SS can also ensure a 'sharp peak' in the gain while the transistor operates as an inverter and improves the signal-to-noise ratio in measurement. The SS can be defined as,³¹

$$SS = \ln(10) \frac{kT}{q} \left(1 + \frac{q^2 D_t}{C_i}\right)$$

where $\frac{kT}{q}$ is the thermal voltage, D_t is the defect trap density ($\text{eV}^{-1}\text{cm}^{-2}$), and C_i is the gate dielectric capacitance (nF cm^{-2}). The reported SS of most solution shearing OSC OFETs is within the range of 100–500 mV Dec⁻¹ on the SiO₂ dielectric.^{11,28,32} To further reduce the SS, a high-quality high- k dielectric developed by atomic layer deposition (ALD) or other methods is needed. Another way to get a small SS is to decrease the trap density of the OSC/dielectric interface. Hydrophobic dielectric is suitable for achieving low trap density, which also helps to improve the device operation stability. However, this is a challenge for solution shearing because of the poor wettability. In a recent report, an extended meniscus printing method can deposit organic crystals onto hydrophobic CYTOP™ surface and a SS value close to the theoretical value of 60 mV Dec⁻¹ has been achieved.¹⁸

Future of Organic Field-effect Transistors

Organic transistors have expanded their application horizon due to the continuous development of new organic molecules, dielectric insulators, and new fabrication methods. With their high gain and biocompatibility, OFETs are highly suitable for next-generation biosensor devices. The functional groups of these sensors can be integrated onto the active layer molecules directly or by using new OFET structures.^{33,34} The use of OFETs at the human-machine interface is another exciting application with significant potential. The structure of the human and animal brain is highly susceptible to rigid interface device components, triggering an immune response and restricting long-term usage. A flexible or even conformal active layer can suppress the immune response and lead to a biocompatible device for long-term application. Miniaturization is another future direction in the development of OFETs and is a critical and essential step towards high device density for advanced functionality like 2D sensor array and circuits. Several critical aspects still need to be addressed in OFET development, including the size of the OFET, the contact effect, the short channel effect, and patterning techniques, requiring breakthroughs in the material system, fabrication process, and device operating physics.

Reference

- (1) Matsui, H.; Takeda, Y.; Tokito, S. *Org. Electron.* **2019**, *75*, 105432.
- (2) Demelas, M.; Lai, S.; Casula, G.; Scavetta, E.; Barbaro, M.; Bonfiglio, A. *Sens. Actuators B Chem.* **2012**, *171*, 198–203.
- (3) Yuvaraja, S.; Nawaz, A.; Liu, Q.; Dubal, D.; Surya, S. G.; Salama, K. N.; Sonar, P. *Chem. Soc. Rev.* **2020**, *49* (11), 3423–3460.

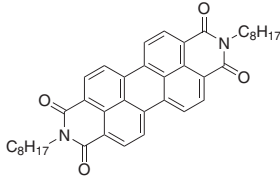
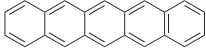
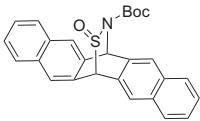
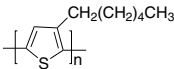
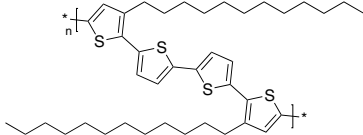
- (4) Mizukami, M.; Oku, S.; Cho, S.; Tatetsu, M.; Abiko, M.; Mamada, M.; Sakanoue, T.; Suzuri, Y.; Kido, J.; Tokito, S. *IEEE Electron Device Lett.* **2015**, *36* (8), 841–843.
- (5) Tang, W.-C.; Hsu, C.-H.; Lin, K.-Y.; Chen, P.-W.; Hsu, Y.-L.; Wang, Y.-L.; Chang, K.-Y.; Chang, Y.-S.; Tsai, C.-C. *Dig. Tech. Pap. - SID Int. Symp.* **2015**, *46* (1), 973–975.
- (6) Subramanian, S.; Park, S. K.; Parkin, S. R.; Podzorov, V.; Jackson, T. N.; Anthony, J. E. *J. Am. Chem. Soc.* **2008**, *130* (9), 2706–2707.
- (7) Pei, K.; Ren, X. C.; Zhou, Z. W.; Zhang, Z. C.; Ji, X. D.; Chan, P. K. L. *Adv. Mater.* **2018**, *30* (13), 1706647.
- (8) Ren, X. C.; Chan, P. K. L. *Appl. Phys. Lett.* **2014**, *104* (11), 113302.
- (9) Chen, M.; Peng, B.; Huang, S.; Chan, P. K. L. *Adv. Funct. Mater.* **2020**, *30* (1), 1905963.
- (10) Janneck, R.; Vercesi, F.; Heremans, P.; Genoe, J.; Rolin, C. *Adv. Mater.* **2016**, *28* (36), 8007–8013.
- (11) Peng, B.; Cao, K.; Lau, A. H. Y.; Chen, M.; Lu, Y.; Chan, P. K. *Adv. Mater.* **2020**, *32* (34), 2002281.
- (12) Yamamura, A.; Watanabe, S.; Uno, M.; Mitani, M.; Mitsui, C.; Tsurumi, J.; Isahaya, N.; Kanaoka, Y.; Okamoto, T.; Takeya, J. *Sci. Adv.* **2018**, *4* (2), ea05758.
- (13) Zhang, Z.; Peng, B.; Ji, X.; Pei, K.; Chan, P. K. L. *Adv. Funct. Mater.* **2017**, *27* (37), 1703443.
- (14) Chen, M.; Peng, B.; Huang, S.; Chan, P. K. L. *U. Adv. Funct. Mater.* **2020**, *30* (1), 1905963.
- (15) Diao, Y.; Tee, B. C.; Giri, G.; Xu, J.; Kim, D. H.; Becerril, H. A.; Stoltenberg, R. M.; Lee, T. H.; Xue, G.; Mannsfeld, S. C. *Nat. Mater.* **2013**, *12* (7), 665–671.
- (16) Duan, S.; Gao, X.; Wang, Y.; Yang, F.; Chen, M.; Zhang, X.; Ren, X.; Hu, W. *Adv. Mater.* **2019**, *31* (16), 1807975.
- (17) Mohammadi, E.; Zhao, C.; Meng, Y.; Qu, G.; Zhang, F.; Zhao, X.; Mei, J.; Zuo, J.-M.; Shukla, D.; Diao, Y. *Nat. Commun.* **2017**, *8*, 16070.
- (18) Kitahara, G.; Inoue, S.; Higashino, T.; Ikawa, M.; Hayashi, T.; Matsuoka, S.; Arai, S.; Hasegawa, T. *Sci. Adv.* **2020**, *6* (41), eabc8847.
- (19) Ferain, I.; Colinge, C. A.; Colinge, J.-P. *Nature* **2011**, *479* (7373), 310–316.
- (20) Kumagai, S.; Watanabe, S.; Ishii, H.; Isahaya, N.; Yamamura, A.; Wakimoto, T.; Sato, H.; Yamano, A.; Okamoto, T.; Takeya, J. *Adv. Mater.* **2020**, *32* (50), 2003245.
- (21) del Pozo, F. G.; Fabiano, S.; Pfaltner, R.; Georgakopoulos, S.; Galindo, S.; Liu, X.; Braun, S.; Fahlman, M.; Veciana, J.; Rovira, C. *Adv. Funct. Mater.* **2016**, *26* (14), 2379–2386.
- (22) Basu, A.; Niazi, M. R.; Scaccabarozzi, A. D.; Faber, H.; Fei, Z.; Anjum, D. H.; Paterson, A. F.; Boltalina, O.; Heeney, M.; Anthopoulos, T. D. *J. Mater. Chem. C* **2020**, *8* (43), 15368–15376.
- (23) Trefz, D.; Gross, Y. M.; Dingler, C.; Tkachov, R.; Hamidi-Sakr, A.; Kiriya, A.; McNeill, C. R.; Brinkmann, M.; Ludwigs, S. *Macromolecules* **2018**, *52* (1), 43–54.
- (24) Sawada, T.; Yamamura, A.; Sasaki, M.; Takahira, K.; Okamoto, T.; Watanabe, S.; Takeya, J. *Nat. Commun.* **2020**, *11* (1), 4839.
- (25) Borchert, J. W.; Zschieschang, U.; Letzkus, F.; Giorgio, M.; Weitz, R. T.; Caironi, M.; Burghartz, J. N.; Ludwigs, S.; Klauk, H. *Sci. Adv.* **2020**, *6* (21), eaaz5156.
- (26) Yamamura, A.; Watanabe, S.; Uno, M.; Mitani, M.; Mitsui, C.; Tsurumi, J.; Isahaya, N.; Kanaoka, Y.; Okamoto, T.; Takeya, J. *Sci. Adv.* **2018**, *4* (2), ea05758.
- (27) Peng, B.; Huang, S.; Zhou, Z.; Chan, P. K. L. *Adv. Funct. Mater.* **2017**, *27* (29), 1700999.
- (28) Kumagai, S.; Yamamura, A.; Makita, T.; Tsurumi, J.; Lim, Y. Y.; Wakimoto, T.; Isahaya, N.; Nozawa, H.; Sato, K.; Mitani, M.; Okamoto, T.; Watanabe, S.; Takeya, J. *Sci. Rep.* **2019**, *9* (1), 15897.
- (29) Deng, W.; Xiao, Y.; Lu, B.; Zhang, L.; Xia, Y.; Zhu, C.; Zhang, X.; Guo, J.; Zhang, X.; Jie, J. *Adv. Mater.* **2020**, *33* (5), 2005915.
- (30) Yamamura, A.; Sakon, T.; Takahira, K.; Wakimoto, T.; Sasaki, M.; Okamoto, T.; Watanabe, S.; Takeya, J. *Adv. Funct. Mater.* **2020**, *30* (11), 1909501.
- (31) Sze, S. M.; Ng, K. K. *Physics of semiconductor devices*. 3rd ed.; Wiley-Interscience: Hoboken, N.J., **2007**; p x, 815 p.
- (32) Makita, T.; Nakamura, R.; Sasaki, M.; Kumagai, S.; Okamoto, T.; Watanabe, S.; Takeya, J. *Adv. Funct. Mater.* **2020**, *30* (39), 2003977.
- (33) Minamiki, T.; Minami, T.; Kurita, R.; Niwa, O.; Wakida, S.-i.; Fukuda, K.; Kumaki, D.; Tokito, S. *Appl. Phys. Lett.* **2014**, *104* (24), 243703.
- (34) Ji, X. D.; Zhou, P. C.; Zhong, L.; Xu, A. M.; Tsang, A. C. O.; Chan, P. K. L. *Adv. Sci.* **2018**, *5* (6), 1701053.
- (35) Duan, S.; Wang, T.; Geng, B.; Gao, X.; Li, C.; Zhang, J.; Xi, Y.; Zhang, X.; Ren, X.; Hu, W. *Adv. Mater.* **2020**, *32* (12), 1908388.

Printable Electrode Materials

Name	Resistivity	Viscosity At 25 °C	Cat. No.
Conductive nanosilver ink for inkjet printing, Silver content: 18-20%W/W	-	10-18 mPa.s (shear rate 1000 s ⁻¹)	907022-25ML
Conductive silver printing ink	volume resistivity 5-6 μΩ-cm	13,000-17,000 mPa.s (at shear rate of 10 sec ⁻¹)	791873-10G 791873-20G
Conductive silver printing ink	volume resistivity 9-10 μΩ-cm	9000-12000 mPa.s (at shear rate of 10 sec ⁻¹)	791881-10G 791881-20G
Conductive silver printing ink	volume resistivity 30-35 μΩ-cm (at a 180°C)	6000-9000 mPa.s (at shear rate of 10 sec ⁻¹)	791903-10G 791903-20G
Copper inkjet ink, Cu(0) in Cu nanoparticles: >95%	-	32 cP (Brookfield, Cone Spindle 40)	907413-5ML
Flexible conductive silver paste for screen printing	Volume resistivity: 925 ohm cm at 60°C 527 ohm cm at 130°C	0.72-1.78 Pa.s (Haake RS1 C20/2° TIL at 230 sec ⁻¹)	901769-25G 901769-100G
Silver, conductive paste	curing temperature 120-150 °C/30-60 min resistivity 1-3 * 10 ⁻⁵ Ω-cm (conductive paste)	100,000-300,000 cP (0.4 rpm Brookfield)	735825-25G
Silver, dispersion, for printing on polyimide films	spec. resistivity ~2.7 μΩ-cm	7-14 cP	736503-25G 736503-100G
Silver, dispersion, for printing on plastic films	spec. resistivity 11 μΩ-cm	10-18 cP	736465-25G 736465-100G
Silver ink, 75 wt%, LIFT printable	-	50,000-100,000 cP (Shear Rate: 1 s ⁻¹) 250cP - 450 cP (Shear Rate: 1000 s ⁻¹)	907669-5G
Silver nanoparticle ink, dispersion in tripropylene glycol mono methyl ether	resistivity ≤7 μΩ-cm (after sintering at 240°C; 4h) resistivity ≤20 μΩ-cm (after sintering at 200°C; 2h)	24 cP	796042-5G 796042-20G
Silver nanoparticle ink, specific gravity 1.53 +/- 0.05 g/ml	resistivity ≤45 μΩ-cm (after sintering at 120 °C, 2h) resistivity ≤7 μΩ-cm (after sintering at 240 °C, 4h) resistivity ≤20 μΩ-cm (after sintering at 200 °C, 2h)	28 cP	798738-10G 798738-25G
SunTronic® silver nanoparticle ink for inkjet printing	resistivity 5-25 μΩ-cm	6-8 cP	901975-2ML 901975-10ML

Organic Semiconducting Materials (Channel)

Name	Structure	Purity, Molecular Weight	Mobility	Cat. No.
5,10-Bis((5-octylthiophen-2-yl)dithieno[2,3-d':2',3'-d'']benzo[1,2-b:4,5-b']dithiophene-2,7-diyl)bis(trimethylstannane)		≥97%	-	901242-250MG
6,13-Bis((triethylsilyl)ethynyl)pentacene		≥99%, HPLC	10 ⁻⁵ cm ² /V·s	739278-100MG 739278-500MG
6,13-Bis(triisopropylsilylethynyl)pentacene		≥99%, HPLC	-	716006-250MG 716006-1G
C8-BTBT		≥99%, HPLC	5.5 cm ² /V·s	747092-100MG 747092-250MG
Dinaphtho[2,3-b:2',3'-f]thieno[3,2-b]thiophene		99%, sublimed grade	2 cm ² /V·s	767638-100MG 767638-500MG

Name	Structure	Purity, Molecular Weight	Mobility	Cat. No.
N,N'-Dioctyl-3,4,9,10-perylenedicarboximide		98%	1.7 cm ² /V·s	663913-1G
Pentacene		≥99.995% trace metals basis, triple-sublimed grade	0.4-3 cm ² /V·s	698423-500MG
		≥99.9% trace metals basis, sublimed grade	0.4-3 cm ² /V·s	684848-1G
		>95.0%, for fluorescence	-	76440-250MG 76440-1G
		99%	0.4-3 cm ² /V·s	P1802-100MG P1802-1G P1802-5G
Pentacene-N-sulfinyl-tert-butylcarbamate		99% (HPLC)	-	699306-100MG 699306-500MG
Poly(3-hexylthiophene-2,5-diyl)		regioregular, average M _w 85,000-100,000	-	900549-1G
		regioregular, average M _w 20,000-45,000	-	900563-1G 900563-5G
		regioregular, average M _w 50,000-75,000	-	900550-1G 900550-5G
PQT-12		average M _w 10,000-25,000	-	906921-500MG



MILLIPORE
SIGMA

subscribe today

Don't miss another topically focused technical review.

It's **free** to sign up for a print or digital subscription of *Material Matters*™.

- Advances in cutting-edge materials
- Technical reviews on emerging technology from leading scientists
- Peer-recommended materials with application notes
- Product and service recommendations



To view the library of past issues or to subscribe, visit SigmaAldrich.com/mm

Nanocharacterization by TEM and AFM

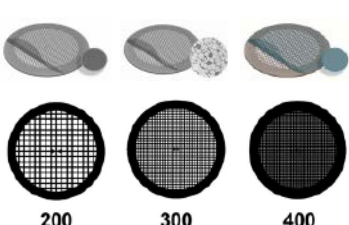


We offer a wide range of TEM and AFM tools, from TEM grids and finders to AFM substrates and grippers.

Available in a wide variety of designs and materials to support your work, select from a broad range of mesh sizes, specimen supporting films, and materials that perfectly suit the conditions of your TEM analysis.

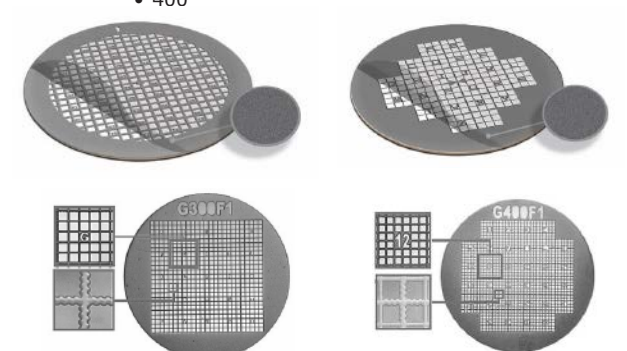
TEM grid specifications:

Material	Mesh Size and Shape	Film Specifications
<ul style="list-style-type: none"> Cu Ni Au Mo Cu/Pd 	<ul style="list-style-type: none"> Square or hexagonal Single-hole grid (75 mm or 100 mm) 100 150 200 300 400 	<ul style="list-style-type: none"> None Continuous formvar film (thicknesses: 5-6 nm, 10 nm) Lacey carbon film (average hole sizes: 50 nm, 100 nm, 150 nm, 100 mm, 150 mm) Continuous amorphous carbon film (thicknesses: 10 nm, 20-30 nm) Continuous formvar/carbon film (thickness: 10nm formvar and 1nm carbon)



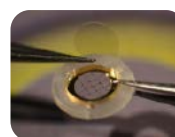
TEM finder grid specifications:

Material	Mesh Size	Film Specifications
<ul style="list-style-type: none"> Cu Ni Au 	<ul style="list-style-type: none"> 135 200 300 400 	<ul style="list-style-type: none"> None Continuous amorphous carbon film (thicknesses: 3-4 nm, 10 nm, 20-30 nm)



Supporting Tools for Nanomaterial Characterization

Our comprehensive range of supporting materials for nanomaterial characterization includes tweezers (sharp tip, disc gripper for AFM), TEM window grids (various thicknesses, 1 or 9 windows), a magnetic pick-up tool, a grid storage box, cryo-capsules, lift-out grids (Cu or Mo), AFM substrates (various dimensions), and much more.



Explore our complete range of TEM grids on:
SigmaAldrich.com/nanocharacterization

© 2021 Merck KGaA, Darmstadt, Germany and/or its affiliates. All Rights Reserved. MilliporeSigma, Material Matters, the vibrant M, and Sigma-Aldrich are trademarks of Merck KGaA, Darmstadt, Germany or its affiliates. All other trademarks are the property of their respective owners. Detailed information on trademarks is available via publicly accessible resources. Lit. No. MS_BR8293EN 0000000 11/2021